ELSEVIER

Contents lists available at ScienceDirect

Desalination

journal homepage: www.elsevier.com/locate/desal



Review of modeling methodologies and state-of-the-art for osmotically assisted reverse osmosis membrane systems

Y.K. Chong ^a, M. Li ^b, D.E. Wiley ^c, D.F. Fletcher ^d, Y.Y. Liang ^{a,*}

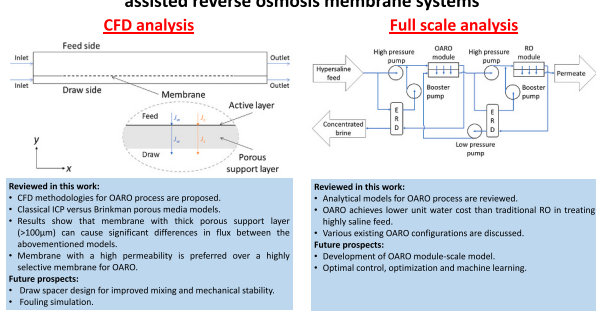
- ^a Faculty of Chemical and Process Engineering Technology, Universiti Malaysia Pahang Al-Sultan Abdullah, Lebuh Persiaran Tun Khalil Yaakob, 26300, Kuantan, Pahang, Malaysia
- ^b Department of Chemical and Materials Engineering, California State Polytechnic University, Pomona, CA 91768, USA
- ^c The University of Newcastle, School of Engineering, Callaghan NSW 2308, Australia
- d The University of Sydney, School of Chemical and Biomolecular Engineering, NSW 2006, Australia

HIGHLIGHTS

- State-of-the-art modeling methodologies for OARO are reviewed.
- CFD for simulating OARO is demonstrated using the classical and porous media models.
- Porous media model is most applicable for a system with a thick membrane.
- Role of mathematical model for OARO module-scale and optimization is highlighted.
- Role of CFD for design of OARO draw spacer and fouling is emphasized.

GRAPHICAL ABSTRACT

Review of modeling methodologies and state-of-the-art for osmotic assisted reverse osmosis membrane systems



ARTICLE INFO

Keywords:
Osmotically assisted reverse osmosis (OARO)
Methodology
Analytical model
Computational fluid dynamics (CFD)

ABSTRACT

Osmotically assisted reverse osmosis (OARO) has been proposed as an innovative solution to recover more water from hypersaline water, surpassing the traditional RO method which is limited by the maximum pressure that the membrane can withstand. An accurate mathematical model is required to elucidate the mechanism of concentration polarization build-up at the inside and outside of the membrane so that these insights can be applied to design an efficient OARO system. This paper reviews state-of-the-art modeling methodologies for OARO using analytical and CFD models. While analytical models have been extensively employed for the design of OARO, the progress of computational models (i.e., CFD) still falls behind. Therefore, CFD methodologies for simulating OARO are demonstrated in this review using the classical and Brinkman porous media models. The sensitivity analysis demonstrates that the Brinkman porous media model is the most applicable for systems with low flux and a thick membrane porous layer. Lastly, future research directions related to OARO modeling are recommended.

E-mail address: yongyeow.liang@umpsa.edu.my (Y.Y. Liang).

^{*} Corresponding author.

Symbols A Water permeability (L m ⁻² h ⁻¹ A_m Membrane area (m ²) B Salt permeability (L m ⁻² h ⁻¹) D Solute diffusivity (m ² s ⁻¹) d_h Hydraulic diameter (m) f_{glob} Global friction factor h Channel height (m) J_w Water flux (L m ⁻² h ⁻¹) J_s Solute flux (L m ⁻² h ⁻¹) k Mass transfer coefficient (m s ⁻¹ k Mass transfer resistance inside L Length (m) k Distance in the normal direction pressure (Pa) k Volumetric flow rate (m ³ s ⁻¹) k Re Reynolds number k Membrane structural parameter k Source term for continuity equivariant k Source term for momentum equal k Source term for mom		w	Solute mass fraction
A Water permeability (L m $^{-2}$ h $^{-1}$ A_m Membrane area (m 2) B Salt permeability (L m $^{-2}$ h $^{-1}$) D Solute diffusivity (m 2 s $^{-1}$) d_h Hydraulic diameter (m) f_{glob} Global friction factor h Channel height (m) J_w Water flux (L m $^{-2}$ h $^{-1}$) k Mass transfer coefficient (m s $^{-1}$ k Mass transfer resistance inside L Length (m) n Distance in the normal direction personal pressure (Pa) Q Volumetric flow rate (m 3 s $^{-1}$) Re Reynolds number S_M Source term for continuity equivalence S_w Source term for momentum equal S_w Source term for mass transfer expected S_w Source term for momentum equal S_w So		x	Distance in the bulk flow direction, parallel to membrane
A_m Membrane area (m²) B Salt permeability (L m²² h²¹) D Solute diffusivity (m² s²¹) d_h Hydraulic diameter (m) f_{glob} Global friction factor h Channel height (m) J_w Water flux (L m²² h²¹) J_s Solute flux (L m²² h²¹) k Mass transfer coefficient (m s² K_{ICP} Mass transfer resistance inside L Length (m) n Distance in the normal direction p Pressure (Pa) Q Volumetric flow rate (m³ s²¹) Re Reynolds number S Membrane structural parameter S_M Source term for continuity equ \vec{S}_u Source term for momentum eq S_i Source term for mass transfer ex S_c Schmidt number Sh Sherwood number t Time (s) t_m Membrane thickness (m) u Velocity (m s²¹)	1 1		surface (m)
B Salt permeability (L m $^{-2}$ h $^{-1}$) D Solute diffusivity (m 2 s $^{-1}$) d_h Hydraulic diameter (m) f_{glob} Global friction factor h Channel height (m) J_w Water flux (L m $^{-2}$ h $^{-1}$) k Mass transfer coefficient (m s $^{-1}$ Kass transfer resistance inside L Length (m) n Distance in the normal direction p Pressure (Pa) Δp Transmembrane pressure (Pa) Q Volumetric flow rate (m 3 s $^{-1}$) Re Reynolds number S_M Source term for continuity equivariant S_w Source term for momentum equals S_w Source term for mass transfer expected S_w Source term for momentum equals S_w Sour	⁻¹ bar ⁻¹)	у	Distance from the membrane surface, in direction normal
DSolute diffusivity $(m^2 s^{-1})$ d_h Hydraulic diameter (m) f_{glob} Global friction factor h Channel height (m) J_w Water flux $(L m^{-2} h^{-1})$ J_s Solute flux $(L m^{-2} h^{-1})$ k Mass transfer coefficient $(m s^{-1})$ K_{ICP} Mass transfer resistance inside L Length (m) n Distance in the normal direction p Pressure (Pa) Δp Transmembrane pressure (Pa) Q Volumetric flow rate $(m^3 s^{-1})$ Re Reynolds number S Membrane structural parameter S_M Source term for continuity equ \vec{S}_u Source term for momentum equ S_i Source term for mass transfer expected and the sum of th			to the surface (m)
d_h Hydraulic diameter (m) f_{glob} Global friction factor h Channel height (m) J_w Water flux (L m $^{-2}$ h $^{-1}$) J_s Solute flux (L m $^{-2}$ h $^{-1}$) k Mass transfer coefficient (m s $^{-1}$ K $_{ICP}$ Mass transfer resistance inside L Length (m) n Distance in the normal direction p Pressure (Pa) Δp Transmembrane pressure (Pa) Q Volumetric flow rate (m 3 s $^{-1}$) Re Reynolds number S Membrane structural parameter S_M Source term for continuity equivariant S_u Source term for momentum equals S_u Source term for mass transfer S_u Source term for momentum equals S_u Source term for mass transfer S_u Source term for momentum equals S_u Source ter)	\boldsymbol{z}	Distance in the direction perpendicular to both x and y (m)
f_{glob} Global friction factor h Channel height (m) J_w Water flux (L m $^{-2}$ h $^{-1}$) J_s Solute flux (L m $^{-2}$ h $^{-1}$) k Mass transfer coefficient (m s $^{-1}$ K I_{CP} Mass transfer resistance inside L Length (m) n Distance in the normal direction p Pressure (Pa) Δp Transmembrane pressure (Pa) Q Volumetric flow rate (m 3 s $^{-1}$) Q Re Reynolds number Q Source term for continuity equivariant Q Source term for momentum equal Q Source term for mass transfer Q Source term for mass transfer Q Source term for momentum equal Q Source term for mass transfer Q Source term for momentum equal Q Source term for		Greek le	attawa
h Channel height (m) J_w Water flux (L m ⁻² h ⁻¹) J_s Solute flux (L m ⁻² h ⁻¹) k Mass transfer coefficient (m s ⁻¹ k Mass transfer resistance inside L Length (m) k Distance in the normal direction k Pressure (Pa) k k Wolumetric flow rate (m ³ s ⁻¹) Re Reynolds number k Reynolds number k Source term for continuity equivalent k Source term for momentum equivalent k Source term for mass transfer expected k Source term for momentum equivalent k Source term for m			
J_{w} Water flux (L m ⁻² h ⁻¹) J_{s} Solute flux (L m ⁻² h ⁻¹) k Mass transfer coefficient (m s ⁻¹ k Mass transfer resistance inside L Length (m) n Distance in the normal direction p Pressure (Pa) Δp Transmembrane pressure (Pa) Q Volumetric flow rate (m ³ s ⁻¹) Re Reynolds number S Membrane structural parameter S_{M} Source term for continuity equivariant S_{u} Source term for momentum equals S_{u} Source term for mass transfer expected S_{u} Source term for momentum equals S_{u} Source term for mass transfer expected S_{u} Sherwood number S_{u} Membrane thickness (m) S_{u} Velocity (m s ⁻¹)		δ	Boundary layer thickness (m)
J_s Solute flux (L m ⁻² h ⁻¹) k Mass transfer coefficient (m s ⁻¹ K_{ICP} Mass transfer resistance inside L Length (m) n Distance in the normal direction p Pressure (Pa) Δp Transmembrane pressure (Pa) Q Volumetric flow rate (m ³ s ⁻¹) Re Reynolds number S Membrane structural paramete S_M Source term for continuity equivariant \overrightarrow{S}_u Source term for momentum equivariant \overrightarrow{S}_u Source term for mass transfer expected \overrightarrow{S}_u Source term for mass transfer expected \overrightarrow{S}_u Schmidt number S_t Schmidt number S_t Membrane thickness (m) t_m Membrane thickness (m) t_m Velocity (m s ⁻¹)		ε	Porosity (2)
kMass transfer coefficient (m s K_{ICP} Mass transfer resistance insideLLength (m)nDistance in the normal directionpPressure (Pa) Δp Transmembrane pressure (Pa)QVolumetric flow rate (m³ s $^{-1}$)ReReynolds numberSMembrane structural paramete S_M Source term for continuity equ \vec{S}_u Source term for momentum eq S_i Source term for mass transfer ex S_c Schmidt number S_h Sherwood numbertTime (s) t_m Membrane thickness (m) u Velocity (m s $^{-1}$)		κ	Darcy permeability of porous support layer (m ²)
K_{ICP} Mass transfer resistance inside L Length (m) n Distance in the normal direction p Pressure (Pa) Δp Transmembrane pressure (Pa) Q Volumetric flow rate (m 3 s $^{-1}$) Q Re Reynolds number Q Source term for continuity equal Q Source term for momentum equal Q Source term for mass transfer Q Source term for mass tra		μ	Dynamic viscosity (Pa s)
LLength (m)nDistance in the normal directionpPressure (Pa) Δp Transmembrane pressure (Pa)QVolumetric flow rate (m³ s⁻¹)ReReynolds numberSMembrane structural parameter S_M Source term for continuity equ \vec{S}_u Source term for momentum eq S_i Source term for mass transfer expected S_c Schmidt number S_h Sherwood numbertTime (s) t_m Membrane thickness (m)uVelocity (m s⁻¹)	s^{-1})	π	Osmotic pressure (Pa)
n Distance in the normal direction p Pressure (Pa) Δp Transmembrane pressure (Pa) Q Volumetric flow rate ($m^3 s^{-1}$) Re Reynolds number S Membrane structural parameter S_M Source term for continuity equ \vec{S}_u Source term for momentum eq S_i Source term for mass transfer expected Sc Schmidt number Sh Sherwood number t Time (s) t_m Membrane thickness (m) u Velocity ($m s^{-1}$)	e the support layer (s m ⁻¹)	ρ	Fluid density (kg m ⁻³)
p Pressure (Pa) Δp Transmembrane pressure (Pa) Q Volumetric flow rate ($m^3 s^{-1}$) Re Reynolds number S Membrane structural paramete S_M Source term for continuity equ \vec{S}_u Source term for momentum eq S_i Source term for mass transfer ex Sc Schmidt number Sh Sherwood number t Time (s) t_m Membrane thickness (m) u Velocity ($m s^{-1}$)		τ	Tortuosity
Δp Transmembrane pressure (Pa) Q Volumetric flow rate (m ³ s ⁻¹) Re Reynolds number S Membrane structural paramete S_M Source term for continuity equ \overrightarrow{S}_u Source term for momentum eq S_i Source term for mass transfer S_i Source term for mass transfer S_i Schmidt number S_i Sherwood number S_i Membrane thickness (m) S_i S_i Welocity (m s ⁻¹)	ion (m)	Subscrip	nts
Q Volumetric flow rate (m ³ s ⁻¹) Re Reynolds number S Membrane structural paramete S_M Source term for continuity equ \overrightarrow{S}_u Source term for momentum eq S_i Source term for mass transfer of sc Schmidt number Sh Sherwood number t Time (s) t_m Membrane thickness (m) u Velocity (m s ⁻¹)		babser 4	Bulk
ReReynolds number S Membrane structural paramete S_M Source term for continuity equ \overrightarrow{S}_u Source term for momentum eq S_i Source term for mass transfer of the source term f)	CECP	Concentrative external concentration polarization
S Membrane structural parameter S_M Source term for continuity equivariant \overrightarrow{S}_u Source term for momentum equal S_i Source term for mass transfer S_i Source term for mass transfer S_i Schmidt number S_i Sherwood number S_i Time (s) S_i Membrane thickness (m) S_i Welocity (m s ⁻¹))	d	Draw side
S_M Source term for continuity equivariant \overrightarrow{S}_u Source term for momentum equations S_i Source term for mass transfer S_i Source term for mass transfer S_i Schmidt number S_i Sherwood number S_i Time (s) S_i Membrane thickness (m) S_i Velocity (m s ⁻¹)		DECP	Dilutive external concentration polarization
\overrightarrow{S}_u Source term for momentum eq S_i Source term for mass transfer S_i Schmidt number S_i Schmidt number S_i Schmidt number S_i Sherwood number S_i Time (s) S_i Membrane thickness (m) S_i Velocity (m s ⁻¹)	ter (m)	eff	Effective
\overrightarrow{S}_u Source term for momentum eq S_i Source term for mass transfer S_i Schmidt number S_i Schmidt number S_i Schmidt number S_i Sherwood number S_i Time (s) S_i Membrane thickness (m) S_i Velocity (m s ⁻¹)	μ	f	Feed side
S_i Source term for mass transfer of S_i Schmidt number S_i Schmidt number S_i Sherwood number S_i Time (s) S_i Membrane thickness (m) S_i Velocity (m s ⁻¹)		j i	Interface between membrane and support layer
Sc Schmidt number Sh Sherwood number t Time (s) t_m Membrane thickness (m) u Velocity (m s $^{-1}$)		ICP	Internal concentration polarization
Sh Sherwood number t Time (s) t_m Membrane thickness (m) u Velocity (m s ⁻¹)	equation (kg iii 3)	in	Inlet
t Time (s) t_m Membrane thickness (m) u Velocity (m s ⁻¹)		int	Intrinsic
t_m Membrane thickness (m) u Velocity (m s ⁻¹)		m	Membrane
u Velocity (m s ⁻¹)		s S	Support layer
-			x-direction
		x	y-direction
\overrightarrow{u} Velocity vector (m s ⁻¹) V_c Volume of the source or sink contraction	aalla (m³)	y z	z-direction

1. Introduction

The evolution of membrane processes throughout history has included several pioneering methods, such as nanofiltration (NF), reverse osmosis (RO), forward osmosis (FO), and pressure retarded osmosis (PRO). Originating in the 1950s, NF/RO involves driving clean water through a semi-permeable membrane to separate solutes for desalination. Later, FO was introduced to use the osmotic gradient to transfer water across the membrane for the pre-treatment process, while PRO was introduced to utilize the pressure difference between the concentrated and dilution solutions for energy generation. These processes have rapidly evolved to address the global water challenges. In recent years, osmotically assisted reverse osmosis (OARO) has gained popularity as an effective method for dewatering hypersaline brine. At high feed salinities, the application of traditional RO to produce pure water is limited as it requires a very high pressure to overcome the transmembrane osmotic pressure. The transmembrane pressure

required to overcome the huge osmotic pressure difference between the feed and permeate sides can easily exceed the membrane burst pressure (i.e., 70 to 80 bar [1]). OARO, in contrast, can overcome this limitation by introducing a dilute solution on the draw side to reduce the osmotic pressure difference. OARO is different from FO/PRO as the former is a pressure driven membrane process in which the hydraulic pressure is applied to drive the water flux from a high concentration feed solution to a low concentration draw solution while the latter are osmotic driven membrane processes in which the water flux is driven by the concentration gradient between a low concentration feed solution and a high concentration draw solution. The schematic diagrams of the membrane processes are shown in Fig. 1.

The OARO concept was first introduced by Loeb and Bloch [2] in 1973 in counter-current flow configuration, but it was limited to only a single stage. Then, in 2017, Bartholomew, et al. [3] proposed the first multi-stage OARO process for the purpose of lowering the concentration of a high salinity feed so that it is within the operating pressure of

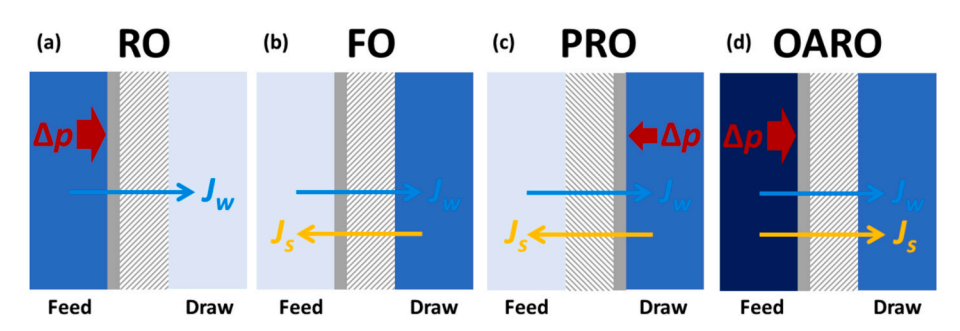


Fig. 1. Schematic diagram of different membrane processes (a) RO, (b) FO, (c) PRO, and (d) OARO. Darker blue indicates a more concentrated solution.

traditional RO. Using this multistage OARO approach, a brine with a very high salinity up to 12.5 wt% can potentially be treated [4], which clearly confirms the potential of OARO for treating brine water.

Unlike traditional RO, OARO not only experiences concentration polarization (CP) and fouling on the feed side but also within the porous layer on the draw side. Moreover, OARO is expected to experience a more severe fouling because the feed concentration treated for OARO (12.5 wt%) is significantly higher than in RO (3 wt%). Therefore, accurate modeling is crucial for a better understanding of the performance of the membrane, as well as for the design and optimization of the system.

The modeling of the membrane desalination process is commonly classified into two categories, namely phenomenological and mechanistic models [5]. The phenomenological model, such as that of Spiegler-Kedem-Katchalsky [6,7], defines the membrane as a black box and describes the mass transfer through irreversible thermodynamics. Phenomenological transport coefficients are used to describe the relationship between the input (i.e., hydraulic pressure and osmotic pressure difference) and output (i.e., water and solute fluxes) of the experiment. Due to the model simplicity, it lacks mechanistic explanations of the effects of transport mechanisms and membrane structures on the fluxes.

On the other hand, a mechanistic model is derived based on the transport mechanisms and membrane structures. This can be achieved either through analytical or numerical methods. Generally, the analytical methods use lumped parameter approaches and do not explicitly resolve the variation of flow velocity and concentrations, while the numerical methods use the distributed parameter approach and resolve the partial differential equations that govern conservation of mass, momentum and energy. Even if local variables are simulated using analytical methods, they are most likely applicable only under low flux conditions [8]. This is because the derivation of existing mass transfer coefficients (measured by the Sherwood number (Sh)) is typically based on the assumption of impermeable wall conditions. Furthermore, employing lumped parameter methods is inadequate for modeling membrane processes on a large scale because they often do not account for the membrane area. Typically, extensive membrane surface area is needed for processes like OARO [3,9], which can lead to significant pressure drops and spatial variations in flux within the membrane channels.

For numerical method, there are two distinct categories: Computational Fluid Dynamics (CFD) modeling and system-level modeling. CFD modeling is based on two-dimensional (2-D) or three-dimensional (3-D) Navier-Stokes equations and diffusion-convection equations and can reveal detailed local hydrodynamics and mass transfer characteristics at the submillimeter scale. However, due to a high computational cost and memory required, this approach is limited to a small fraction of the membrane (millimeter scale) and is not well suited for a whole system (meter scale). The system-level model is typically based on an algebraic equation or one-dimensional (1-D) ordinary differential equations (ODEs) that can be easily solved to predict and optimize system performance. For the system-level model to be accurate, the modeling parameters, such as friction coefficient and mass transfer coefficient, should be derived from CFD and/or experiments. Therefore, both are important to advance OARO design and application. Table 1 summarizes the advantages and limitations of both modeling approaches.

When Bartholomew, et al. [3] first introduced the multistage OARO, it was purely based on an analytical model to determine the practicality of this new technology. The reliability of this analytical model was demonstrated and verified in several experimental studies [10–13]. Since its inception over the last six years, the analytical model has been progressively used in parametric studies [3,14,15], techno-economic analysis [4,16,17] and evaluation of different OARO configurations [15,18–21]. The second modeling approach (i.e., CFD), on the other hand, still falls behind for OARO application owing to the complex interaction between the solute concentration and flux inside and outside

 Table 1

 Advantages and limitations of analytical and numerical models.

Methods	Advantages	Limitations
Analytical model	Simple and easy to use. Allows quick understanding of the interplay between operating variables, membrane structures, and desalination performance.	 The prediction of external mass transfer is limited to low flux conditions as the generalized <i>Sh</i> correlation is typically derived under impermeable wall conditions. Often neglects the impact of membrane area which could leads to excessive pressure drop and spatial variation of flux along the channel.
Numerical model	 Boundary conditions are well controlled. Local hydrodynamic and concentration profiles are revealed. 	For CFD, in-depth knowledge is required.

of the membrane.

The objectives of this paper are to review existing analytical modeling work related to OARO since 2017 and to establish CFD methodologies for modeling the flow and solute for an OARO system. In addition, this review will highlight the capabilities and limitations of both methodologies. This review is organized in four sections. First, fundamental knowledge about OARO modeling, such as common model assumptions, and operating and membrane parameters are explained in Sections 2.1 and 2.2, respectively. Second, the methodology for determining the fluxes and concentration polarization (CP) in a full-scale system using analytical models are discussed and established in Section 2.3. Section 2.4 focuses on simulating and establishing the local water flux and CP using CFD models based on classical internal CP (ICP) developed by Loeb, et al. [22] and Brinkman porous media approaches. The reliability of both models in terms of water flux is determined. Third, the current state-of-the-art of OARO analytical modeling work is reviewed in Section 3. Finally, the future directions for OARO modeling studies are highlighted in Section 4.

2. Modeling methodologies

2.1. Physical and fluid properties model assumption

Several assumptions have to be made in modeling OARO to simplify this complex membrane process. Generally, even though osmotic pressure increases proportionally with temperature, an isothermal system can be assumed as OARO does not involve any significant energy transfer as heat. Therefore, the temperature of the system should remain relatively constant during the process [23]. However, this assumption should be carefully considered as the increase of temperature can lead to an increase of the mass transfer coefficient [24], which could affect the flux calculation. Furthermore, the system can be assumed to involve Newtonian fluids, which display a linear relationship between the shear stress and shear rate.

As the flux for OARO is typically small [3], the overall changes in the diffusivity and viscosity are small. Therefore, constant solution properties, such as viscosity and diffusivity, can be assumed in the mathematical model [25]. However, if the flux value approaches those of typical ultrafiltration, it is important to consider the effects of viscosity variation [26]. It was also reported elsewhere that the density variation due to the solute concentration difference between the feed and membrane surface was insufficient to create notable buoyancy effects when the flow direction is normal to the direction of gravity [27]. Therefore, the density of the fluid can be assumed as constant in a horizontal channel. Furthermore, gravity has little impact on the flow solution inside the channel [27].

2.2. Operating and membrane model parameters

Mathematical modeling of the OARO process requires operating and membrane parameters as inputs. The most important membrane parameters are the water permeability (A), the solute permeability (B) and the membrane structural parameter (S), which must be obtained experimentally [28]. The most common experimental method used for this purpose is the RO-FO methods [29–31]. First, A and B are determined through RO tests. Next, S is determined through FO tests based on A and B obtained from the RO tests. This form of S is known as the effective structural parameter ($S_{\rm eff}$). S can also be defined as the result of multiplying the membrane thickness (t_m) and tortuosity (τ) , divided by porosity (ε). This form of S is known as the intrinsic structural parameter (S_{int}) . The porosity (ε) of the membrane support layer can be determined by using either gravimetric analysis [32] or imaging characterization techniques, such as scanning electron microscopy (SEM) [33], confocal laser scanning microscopy (CLSM) [34] and x-ray computed tomography (XCT) [35].

It is crucial to review the methods used for characterizing structural parameters to ensure accurate outcomes. For instance, calculating the $S_{\rm eff}$ based on lumped parameters might overlook the significant variations at different positions. This bulk averaging method does not capture how asymmetry could affect mass transfer locally. Moreover, accurately capturing the intrinsic properties of the support layer is crucial in determining the $S_{\rm int}$. Users should be aware of the drawbacks of the techniques used to capture these intrinsic properties to avoid introducing biases. Interested readers can refer to the review article of Manickam and McCutcheon [36] to understand more about the drawbacks of the intrinsic property measurement techniques.

Determination of osmotic pressure is one of the crucial parameters in any osmotically driven process. One of the most common assumptions in determining osmotic pressure is the adoption of the ideal linear Van't Hoff approximation. As such, the osmotic pressure is directly proportional to solute mass fraction in a single solute system. However, it should be noted that the linear approximation of osmotic pressure is only valid for dilute solute concentration up to a certain limit [37]. Beyond this limit, the actual osmotic pressure deviates significantly from the ideal value, as reported by Scatchard, et al. [38] and Rogers and Pitzer [39]. Therefore, a polynomial trendline should be used instead to predict the non-linear correlation between the osmotic pressure and solute mass fraction as discussed in detail by Bartholomew, et al. [4] and Beni, et al. [20].

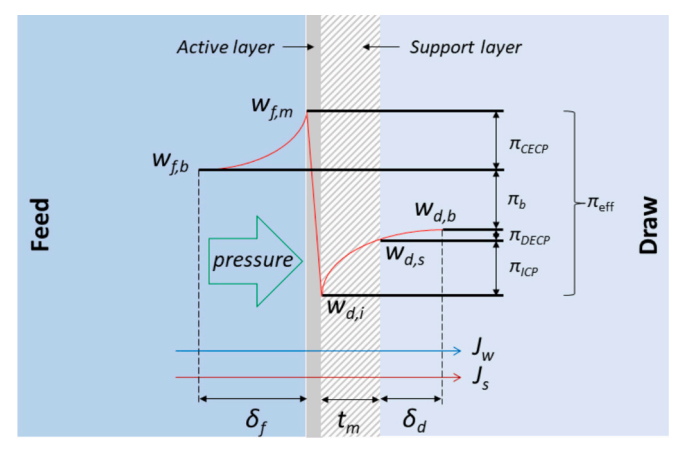


Fig. 2. Schematic diagram of an asymmetric membrane.

2.3. Analytical model for determining water flux, solute flux and individual osmotic pressure across OARO compartments for a full-scale system

Fig. 2 shows the solute mass fraction profile across a semi-permeable membrane in OARO mode. For OARO, it is worth noting that the effective osmotic pressure difference (π_{eff}) is higher than the bulk osmotic pressure difference (π_b). The bulk draw solute mass fraction ($w_{d,b}$) is reduced to $w_{d,s}$ on the support layer and subsequently $w_{d,i}$ at the membrane-support layer interface due to the dilution with incoming water while the bulk feed solute mass fraction ($w_{f,b}$) is elevated to $w_{f,m}$ on the membrane surface due to the solute accumulation caused by the membrane rejection. The governing diffusive and convective components can be integrated across t_m and the boundary layers on the feed (δ_f) and draw (δ_d) sides to obtain the $w_{d,i}$, $w_{d,s}$ and $w_{f,m}$.

One of the important discussions in modeling CP is the relative importance of ICP between RO and OARO. It was argued that the ICP in RO mode is negligible because water flux (J_w) and solute flux (J_s) flow in the same direction [40]. However, the same argument cannot be applied for OARO, where the stream in the draw side of OARO is not clean water and contains a significant amount of solutes. Therefore, the water flux passing through the porous layer causes dilution, leading to dilutive ICP.

Hence, J_w and J_s for OARO can be calculated as a function of solute mass fraction difference for both sides of membrane $(w_{f,m} - w_{d,i})$ and the other parameters (i.e., transmembrane pressure (Δp) , π , A and B).

$$J_{w} = A \left(\Delta p - \pi \left[\frac{w_{f,b} exp\left(\frac{J_{w}}{k_{f}}\right) - w_{d,b} exp\left(-J_{w}\left[K_{ICP} + \frac{1}{k_{d}}\right]\right)}{1 + \frac{B}{J_{w}}\left(exp\left[\frac{J_{w}}{k_{f}}\right] - exp\left[-J_{w}\left(K_{ICP} + \frac{1}{k_{d}}\right)\right]\right)} \right] \right)$$
(1)

$$J_{s} = B \left[\frac{w_{f,b} exp\left(\frac{J_{w}}{k_{f}}\right) - w_{d,b} exp\left(-J_{w}\left[K_{ICP} + \frac{1}{k_{d}}\right]\right)}{1 + \frac{B}{J_{w}}\left(exp\left[\frac{J_{w}}{k_{f}}\right] - exp\left[-J_{w}\left(K_{ICP} + \frac{1}{k_{d}}\right)\right]\right)} \right]$$
(2)

It should be noted that K_{ICP} refers to the mass transfer resistance inside the support layer while k_f and k_d refer to mass transfer coefficients at the feed and draw sides, respectively. Readers are encouraged to refer to [41] for a detailed derivation of these equations for J_w and J_s . Nevertheless, Eqs. (1) and (2) with lumped parameters are insufficient to describe the full-scale membrane process because both J_w and J_s vary in a scaled-up system due to the significant decrease of driving force along the membrane length.

Therefore, multi-scale modeling that combines micro- and module-scale models is required to describe the full-scale membrane process under actual operating. First, the correlation for the mass transfer coefficient (k) and friction factors ($f_{\rm glob}$) needs to be obtained from a CFD simulation to describe the mass and momentum transfers inside the channel at the microscopic level (submillimeter scale). These correlations can then be incorporated into the ordinary differential equations (ODE) derived from first principles (as shown in Eqs. (3) to (7)) to predict the change of flow, solute concentration and pressure loss at the module-scale (meter) for a single membrane wall:

$$\frac{\partial Q_f}{\partial x} = -\frac{A_m J_w}{I} \tag{3}$$

$$\frac{\partial (Q_f w_{f,b})}{\partial x} = -\frac{A_m J_s}{L} \tag{4}$$

$$\frac{\partial Q_d}{\partial x} = \frac{A_m J_w}{L} \tag{5}$$

$$\frac{\partial (Q_d w_{d,b})}{\partial x} = \frac{A_m J_s}{L} \tag{6}$$

$$\frac{\partial p}{\partial x} = -\frac{2\rho u_{\text{eff}}^2}{d_h} f_{\text{glob}} \tag{7}$$

where Q is the volumetric flow rate, A_m is the membrane area, L is the module length, p is the pressure, ρ is the density, $u_{\rm eff}$ is the effective velocity and d_h is the hydraulic diameter. $f_{\rm glob}$ is the Fanning friction coefficient in the feed channel. The subscripts b, f and d represent bulk, feed and draw sides, respectively.

It should be noted that the k values for both the feed and draw channels are dependent on the operating conditions and geometry. Table 2 lists all the Sh correlations used for OARO to date. Re is the Reynolds number and Sc is the Schmidt number. There are shortcomings in the existing correlations: 1) limited flux condition [42] and 2) valid for only feed side but not draw side because correlations [43,44] are developed based on a net-type spacer and they will probably not be applicable for the tricot spacer that is typically applied in the OARO permeate side. Therefore, CFD should be used to derive hydrodynamic and mass transfer correlations based on the given operating conditions and geometry.

2.4. CFD model for determining local water flux and solute concentration

It should be noted that modeling of flow across the support layer of a membrane is a challenging task because its intrinsic support properties, such as ε and τ , vary with position in most real systems. Although it was reported elsewhere that the spatial variations of the pore structure can be modeled through the CFD, some unrealistic assumptions were adopted (i.e., τ equal to unity [46]). Another approach for simulating flow across the support layer is by assuming the support layer as isotropic, in which the local intrinsic membrane properties can be lumped into a single representative measure (i.e., A, B, ε and τ). Section 2.4.1 validates the mathematical models based on isotropic membrane properties with experimental data. However, to date, it remains unclear to what extent this assumption can be safely applied. There is no limitation in CFD to modeling spatially varying properties if suitable data are available. Further studies are needed to understand the impacts of this assumption on the accuracy of the mathematical models.

Assuming spatially constant membrane properties, the hydrodynamics and mass transfer inside the membrane porous support layer can be modeled using the Brinkman equation via the following continuity, momentum, and mass transfer governing equations:

$$\frac{\partial(\rho\varepsilon)}{\partial t} + \nabla \cdot (\rho\varepsilon \overrightarrow{u}) = S_M \tag{8}$$

$$\frac{\partial(\rho\varepsilon\overrightarrow{u})}{\partial t} + \nabla(\rho\varepsilon\overrightarrow{u}\otimes\overrightarrow{u}) = \nabla\cdot(\mu\varepsilon(\nabla\overrightarrow{u} + \nabla\overrightarrow{u}^T)) - \frac{\mu}{\kappa}(1-\varepsilon)\overrightarrow{u} - \varepsilon\nabla p + \overrightarrow{S}_u$$

$$\frac{\partial(\rho\varepsilon w)}{\partial t} + \nabla \cdot (\rho\varepsilon w \overrightarrow{u}) = \nabla \cdot (\rho D^* \nabla w) + S_i$$
(10)

where \overrightarrow{u} is the velocity vector, t is the time, μ is the dynamic viscosity, κ is the Darcy's permeability coefficient of the porous support layer and w is the solute mass fraction. The value of ε is <1 for the porous support layer. On the other hand, for empty feed and draw channels, ε is equal to 1 and the viscous drag term in the momentum governing equation is

Table 2 *Sh* correlation in different channel geometries.

Ref.	Geometry	Flow	Sh correlation for k
[45]	Empty channel	Laminar	$Sh = 1.85 \left(ReSc \frac{d_h}{L} \right)^{0.33}$
[45]	Empty channel	Turbulent	$Sh = 0.04Re^{0.75}Sc^{0.33}$
[43]	Net-type spacer-filled channel	Laminar	$Sh = 0.46 (ReSc)^{0.36}$
[44]	Net-type spacer-filled channel	Laminar	$Sh = 0.2Re^{0.57}Sc^{0.4}$

absent. In addition, D^* varies according to the regions. For empty channels, D^* is equal to the diffusivity (*D*), whereas for the porous support layer region, D^* is equal to the effective diffusivity (D_{eff}).

 S_M , \overrightarrow{S}_u and S_i are the source terms used for the above equations that represent the flux across the membrane wall (Fig. 3):

$$S_M = \frac{\rho A_m J_w}{\varepsilon V_c} \tag{11}$$

$$\overrightarrow{S}_{u} = S_{M} \overrightarrow{u} \tag{12}$$

$$S_i = \frac{\rho A_m J_s}{\varepsilon V_c} \tag{13}$$

where V_c is the volume of the source or sink cells. The source term, \overrightarrow{S}_u , is often neglected due to the low velocity in the boundary layer.

On the other hand, the CFD model based on the classical analytical ICP model developed by Loeb, et al. [22] does not resolve the membrane thickness explicitly. Instead, it uses an analytical ICP model to predict the $w_{d,i}$ and subsequently J_w and J_s . Readers should refer to [41] to get detailed information of this model.

Table 3 outlines the boundary conditions for the remaining non-membrane regions.

One of the main strategies to reduce numerical error in CFD is the use of the correct meshing technique. For empty channels, structured meshes are preferred as they offer simplicity and more precise results relative to unstructured meshes [47]. However, for complex domains like spacer-filled channels, unstructured meshes are desired. Therefore, the mesh qualities, such as skewness and orthogonality, should be checked [48]. Furthermore, generating a sufficient number of inflation layers on the membrane surface is important to ensure the velocity and solute gradients are captured accurately [48].

2.4.1. Validity of OARO CFD model based on classical ICP and Brinkman porous media approaches and sensitivity analysis

The validation process involves comparing the mathematical model with experimental results. This step is essential for a CFD model to ensure its accuracy and agreement with physical reality. Fig. 4 shows that the classical ICP and Brinkman models tested for OARO give similar J_w results. In addition, the classical ICP [41] and Brinkman models demonstrate a good agreement with reported experimental J_w measurements by Chen, et al. [10]. However, a larger difference between the experimental results and the CFD models is observed at a higher Δp . These observations are consistent with the outcomes reported by Chen, et al. [10], whose analytical model showed similar J_w at a lower Δp but exhibited a larger deviation at a higher Δp . They attributed this deviation at high Δp to the constraints of their membrane characterization method in accurately determining B [10]. The membrane parameters and operating conditions of Chen, et al. [10] experiment are summarized in Table 4.

In addition, the classical ICP and Brinkman models tested for OARO give similar flux results (Fig. 4). However, in the classical ICP model, membrane thickness is not explicitly resolved in the domain but instead, Loeb, et al. [22] used an analytical ICP model to simulate the flow and solute fraction inside the porous support. Therefore, in extreme conditions, the simplifications in this model, such as negligible viscous drag effects on flow velocity, may cause inaccuracies in predicting the solute fraction within the porous support. To understand how changes in thickness impact J_w between the two models, a sensitivity analysis was conducted by varying this parameter by ± 50 %. As the typical thickness of the osmotic membrane lies within 50 to 150 µm [11,49–51], a baseline value of 100 µm is set. The other parameters are provided in Table 5.

The water flux calculated using the classical ICP ($J_{w,classical}$) and Brinkman porous media models ($J_{w,porous\ media}$) is determined based on the boundary conditions specified in Table 3. The relative change in the

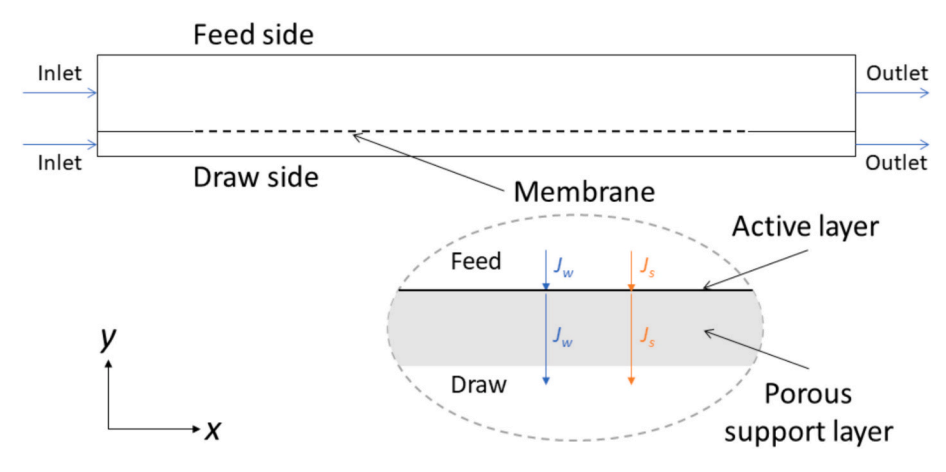


Fig. 3. Schematic diagram of the membrane and channels for the CFD.

Table 3CFD boundary conditions using classic analytical ICP and Brinkman porous media model.

		Equations	
Locations	Boundary conditions	Classic analytical ICP model	Brinkman porous media model
Inlet	Parabolic velocity profile	$u_{y} = 6u_{in}\frac{y}{h}\left(1 - \frac{y}{h}\right)$	
	Uniform solute mass fraction	$w = w_b, \frac{dw}{dy} = \frac{dw}{dz} = 0$	
Outlet	Zero gauge pressure	$p_{gauge} = 0$	
Non- membrane	No-slip	$p_{gauge} = 0$ $u_x = u_y = u_z = \frac{dw}{dn} = 0$	
Membrane	Water permeation	$J_{W} =$	$J_{w} = A(\Delta p - \pi [w_{f,m} - w_{d,i}])$
		$A\left(\Delta p - \pi \left[\frac{w_{f,m} - w_{d,s}exp(-J_wK_{ICP})}{1 + \frac{B}{J_w}(1 - exp[-J_wK_{ICP}])}\right]\right)$	
	Salt permeation	$J_{s} = B \left[\frac{w_{f,m} - w_{d,s} exp(-J_{w}K_{ICP})}{1 + \frac{B}{J_{w}}(1 - exp[-J_{w}K_{ICP}])} \right]$	$J_s = B(w_{f,m} - w_{d,i})$
Porous support		-	ε < 1 for porous region in Eqs. (8) to (10). ε is the intrinsic value of the membrane porous support.

water flux (ΔJ_w) in comparison with the base case (Brinkman porous media model) is given as defined in Eq. (14):

$$\Delta J_{w} = \frac{J_{w.classical} - J_{w.porous\ media}}{J_{w.porous\ media}} \times 100\% \tag{14}$$

Interestingly, the ΔJ_w remains small when the thickness is 100 µm (0 % of Δt_m), but it exceeds 24 % as the thickness of the membrane increases by 50 %, as shown in Fig. 5. The classical ICP model also tends to overpredict the measured water flux in comparison with the Brinkman porous media model because the former does not consider the viscous drag in the porous media, leading to negligible flow resistance and an exaggerated permeate velocity.

2.4.2. A comparative analysis of the impact of membrane permeability (A) and selectivity (A/B) on OARO performance

To date, there remains a need for optimizing the membranes employed in OARO. The traditional RO membrane might not be the optimal choice for OARO due to its large thickness. The large thickness can give rise to increased ICP, subsequently leading to a decline in membrane flux. Therefore, an osmotic membrane is normally preferred over an RO membrane in the current OARO study [11,12,55] due to its lower thickness, which helps mitigate the ICP.

Currently, the understanding of molecular-level transport through dense polymer layers is still limited [56]. Consequently, there is a pressing need for a thorough grasp of how membrane synthesis and structure impact performance in order to enhance membrane selectivity.

In this context, it is noteworthy that the recent development of an open access resource, known as the Open Membrane Database [56], is starting to address this need. This database contains comprehensive information regarding the latest reverse osmosis (RO) membranes, sourced from peer-reviewed journals, patents, and commercial product data, which holds significant value for advancing membrane development.

An ideal membrane should have high permeability and high selectivity. However, this is difficult to achieve because enhancing the water permeability almost inevitably results in significant increase of the solute permeability, consequently reducing selectivity [57]. Therefore, a thoughtful decision should be made between prioritizing high permeability or high selectivity in the selection and development of OARO membranes, unless a new material can be found in which a different balance can be found between the permeability and selectivity, as is common in the search for better gas transport membranes where the search for new materials is driven by breaking the so-called 'Robeson upper bound' [58].

Nevertheless, some recent advanced membrane technologies, such as energy-efficient reverse osmosis (EERO) [59,60] (Fig. 6a) and low salt rejection reverse osmosis (LSRRO) [61] (Fig. 6b), have been proposed to utilize low-selectivity membranes to overcome the challenge of osmotic pressure difference. In the EERO process, the retentate from reverse osmosis is fed into a countercurrent membrane cascade with recycle (CMCR) consisting of one or a few stages of NF to further concentrate the retentate and recover more water. EERO offers the benefit of reducing the osmotic pressure differential by at least 33 % compared with single-

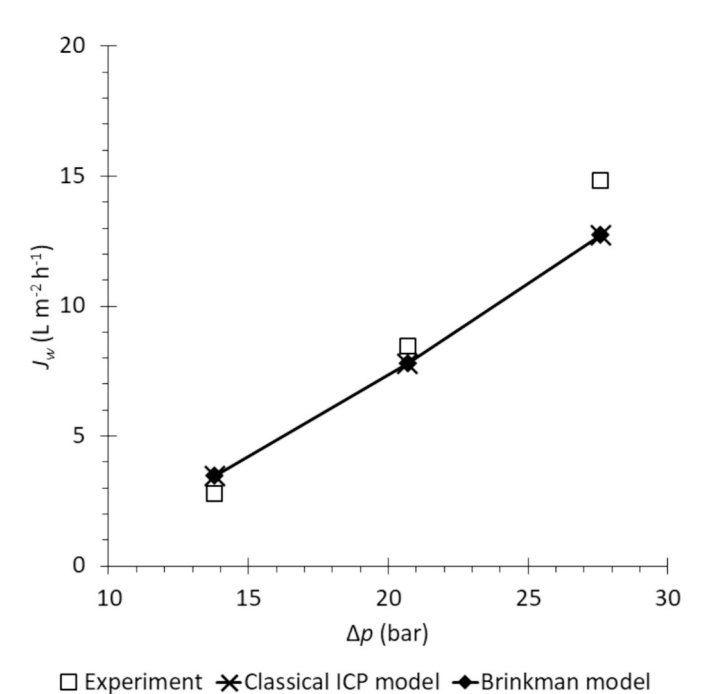


Fig. 4. Dependence of J_w on Δp . The square marks indicate the results obtained from Chen, et al. [10] experimentally, the asterisk and diamond marks indicate the result obtained from classical ICP [41] and Brinkman CFD models, respectively.

Table 4Membrane parameters and operating conditions of Chen, et al. [10] experiment.

Parameter	Values
Water permeability, A (L m ⁻² h ⁻¹ bar ⁻¹)	2.99
Solute permeability, <i>B</i> (L m ⁻² h ⁻¹)	2.03
Membrane structural parameter (μm)	394.5
Transmembrane pressure, Δp (bar)	13.8, 20.7 & 27.6
Bulk feed solute mass fraction, $w_{f,b}$	0.034
Bulk draw solute mass fraction, $w_{d,b}$	0.023
Feed channel inlet velocity, $u_{f.in}$ (m s ⁻¹)	0.15
Draw channel inlet velocity, $u_{d,in}$ (m s ⁻¹)	0.19
Membrane length, L_m (m)	0.076
Feed channel height, h_f (m)	0.003
Draw channel height, \hat{h}_d (m)	0.0005

Table 5 Parameters for the sensitivity analysis.

Parameter	Values	Reference
Water permeability, A (L m ⁻² h ⁻¹ bar ⁻¹)	1.80	[11,12,50]
Solute permeability, <i>B</i> (L m ⁻² h ⁻¹)	0.54	[11,12,50]
Porosity of the porous support layer, ε	0.5	[52–54]
Tortuosity of the porous support layer, τ	2	[52–54]
Transmembrane pressure, Δp (bar)	25	[10]
Bulk feed solute mass fraction, $w_{f,b}$	0.05	[10]
Bulk draw solute mass fraction, $w_{d,b}$	0.03	[10]
Feed channel inlet velocity, $u_{f,in}$ (m s ⁻¹)	0.12	[10]
Draw channel inlet velocity, $u_{d,in}$ (m s ⁻¹)	0.12	[10]

stage RO at the same water recovery rate [59]. Additionally, the specific energy consumption (SEC) of EERO can be lower than that of single-stage RO at water recovery above the critical threshold (58.5 % for 3-stage EERO and 75 % for 4-stage EERO) [60]. In LSRRO, the retentate from reverse osmosis is fed into subsequent stages with low salt rejection RO or NF membranes to further concentrate the retentate and recover more water. LSRRO requires substantially less energy than traditional thermally-driven phase change-based technologies, such as mechanical

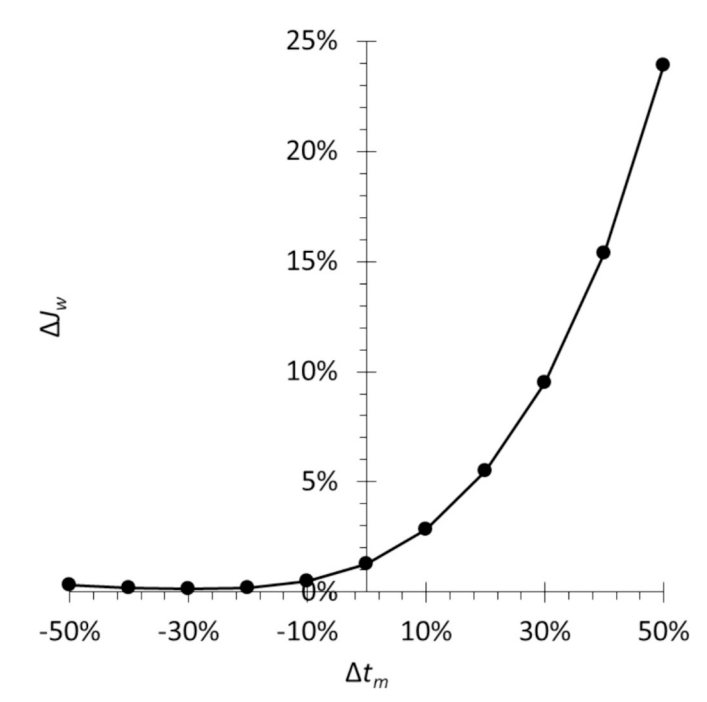


Fig. 5. Results of the sensitivity analysis performed using the CFD model described above.

vapor compression (MVC), to concentrate the brine. For example, it has been reported elsewhere [61] that to concentrate a saline feed stream from 0.1 to 1.0 M NaCl, the SEC of LSRRO is four times lower than that of MVC.

Unlike traditional RO, the membrane selectivity is not as important for OARO because perfect solute rejection is not required. Furthermore, in OARO, the feed solute mass fraction is higher than the draw solute mass fraction. Consequently, unlike in FO or PRO, reverse solute flux (RSF) does not occur in OARO as the directions of the water and solute fluxes are the same. Thus, any reduction in membrane selectivity will not adversely affect water flux; rather, it will potentially enhance water flux because the leakage of solute from the feed side to the draw side will lower the osmotic pressure difference across the membrane [15].

A CFD simulation with the Brinkman model was conducted for this paper to evaluate J_w and the solute fraction of permeate flux (w_p) in OARO by varying the A and A/B. Prior to determining the A and A/B used in this simulation, an upper bound relationship for the trade-off between permeability and selectivity was established (Fig. 7) based on data for existing conventional membranes available in the market (commercial), as well as advanced membranes developed by researchers for their studies (novel) (listed in Table S1). It was found that A/B is inversely proportional to the square of A ($A/B \propto A^{-2}$) which is the same as reported elsewhere [62,63]. Using Fig. 7, the best possible membrane at the present point in time was identified. The membrane parameters used in the simulation are provided in Table 6.

As A and B can change by several orders of magnitude (0.1 to 10 L m $^{-2}$ h $^{-1}$ bar $^{-1}$ [64,65] and 0.01 to 1 L m $^{-2}$ h $^{-1}$ [10,66], respectively), the simulations are conducted at different magnitudes of A and B (shown in Table 6) along the upper bound. In OARO, it was found that J_w increases as A increases and A/B decreases (see Fig. 8a). However, w_p also rises sharply as A/B decreases, as shown in Fig. 8b. This occurs because as A/B decreases, B increases, leading to a higher J_s . Therefore, while a membrane exhibiting a high permeability is favored over a highly selective membrane, it is important to note that a reduced selectivity can potentially cause excessive solute leakage.

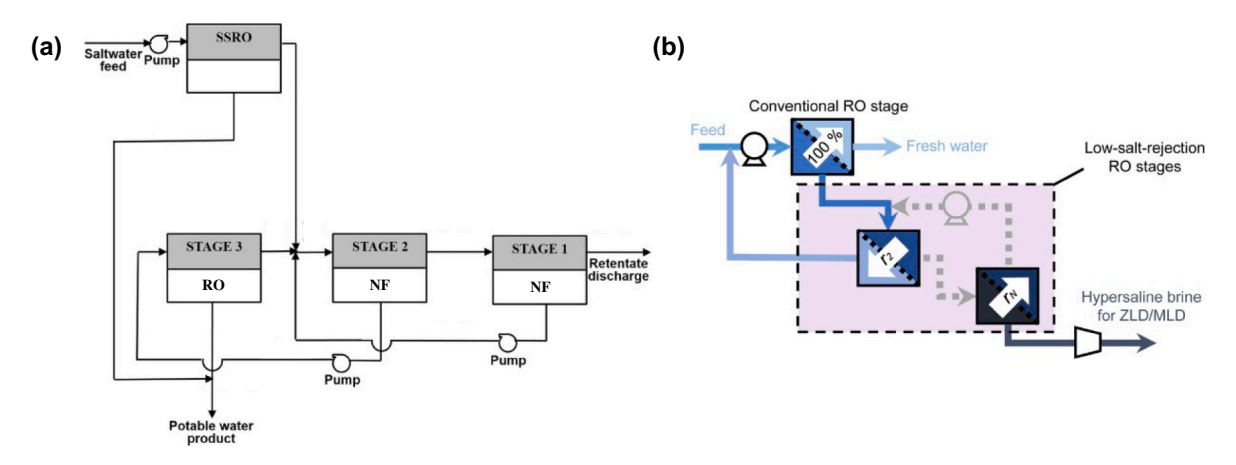


Fig. 6. Schematic diagrams of (a) energy-efficient reverse osmosis (EERO) [59,60] and (b) low salt rejection reverse osmosis (LSRRO) [61].

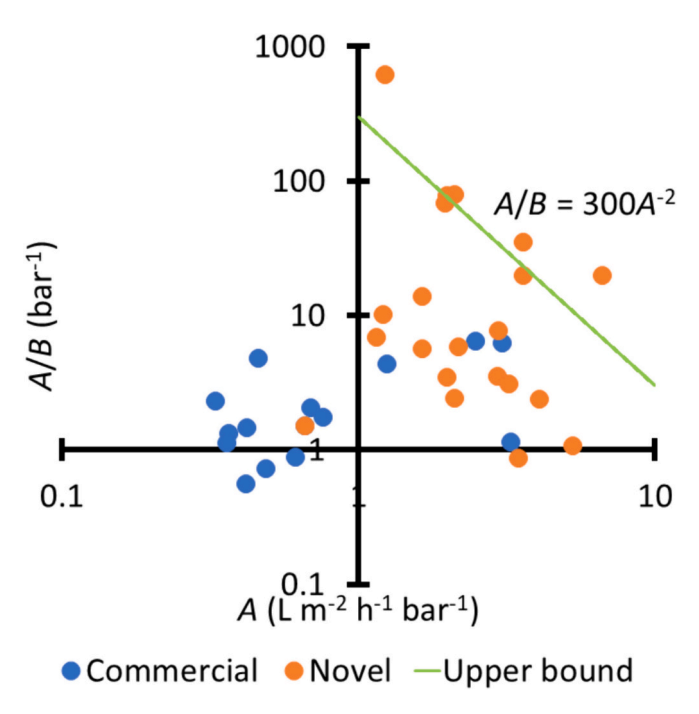


Fig. 7. Permeability-selectivity trade-off relationship for state-of-the-art osmotic membranes. Notes: The readers are referred to the data points and sources in the Supplementary material.

 $\begin{tabular}{ll} \textbf{Table 6} \\ The membrane parameters for OARO membrane analysis. The permeabilities and selectivity are decided based on the trendline of the trade-off upper bound relationship obtained from Fig. 7. \\ \end{tabular}$

Parameter	Values	Reference
Water permeability, A (L m ⁻² h ⁻¹ bar ⁻¹)	2, 4, 6 & 8	_
Solute permeability, B (L m ⁻² h ⁻¹)	0.03, 0.21, 0.72 & 1.71	_
Selectivity, A/B (bar ⁻¹)	75.0, 18.8, 8.3 & 4.7	_
Structural parameter, S (µm)	500	[12,51]
Transmembrane pressure, Δp (bar)	30	[10]
Bulk feed solute mass fraction, $w_{f,b}$	0.05	[10]
Bulk draw solute mass fraction, $w_{d,b}$	0.03	[10]
Feed channel inlet velocity, $u_{f,in}$ (m s ⁻¹)	0.15	[10]
Draw channel inlet velocity, $u_{d,in}$ (m s ⁻¹)	0.15	[10]

3. Current state of mathematical modeling

3.1. Validation of existing analytical model

To date, only a limited number of OARO experiments have been conducted to validate the analytical model [10-13], which were claimed to have good agreement with the experimental results. To simplify the model, the external CP (ECP) at the draw side is often assumed to be negligible, as its impact is much smaller than that of the ICP. However, at a higher Δp , there is a greater deviation in water flux between the analytical model and experiment [10,11]. It is noteworthy that the water flux calculated by the analytical model consistently overpredicts those observed in the experiments [10,11]. The discrepancy was attributed to the limitations in the membrane characterization method used to determine B [10], as well as changes in S under pressurized conditions [11]. Moreover, the currently available analytical model is limited to a membrane module without a feed spacer. This is because the generalized Sh-correlation used in these studies is limited to the empty channel. In the case of a membrane module with a spacer, the correlation will depend significantly on the spacer geometry. Therefore, CFD needs to be employed to formulate an Sh correlation for the different spacer geometry.

As shown in Table 7, the mathematical modeling of OARO has been extensively validated in lab-scale experiments. However, the model validation of this recent advanced membrane technology in real-world applications is still lacking. Only recently, a pilot study in a multistage system consisting of NF, RO, and OARO has been reported [67]. More effort needs to be made to validate the mathematical modeling at larger scale.

3.2. Mathematical model for parametric study

A modeling approach that allows the membrane or operating parameters to be varied offers flexibility in finding the optimal conditions. It was reported that one of the easiest way to reduce the number of stages required is by increasing the feed pressure so that a higher water recovery can be achieved [14]. Additionally, using a lower flow rate is more desirable as it results in higher water recovery and requires lower energy consumption [14] at the expense of a higher fouling tendency [68]. It is worth noting that the porosity of the draw side is typically smaller than that of the feed side because the draw side needs to withstand the high transmembrane pressure. As such, maintaining a lower ratio of draw to feed inlet flow rates is recommended to prevent excessive pressure loss in the draw stream [14]. Nevertheless, if the draw flow rate is too low, the decrease of draw solute fraction along the membrane channel can become significant which results in the increase of osmotic pressure difference, leading to the increase of transmembrane

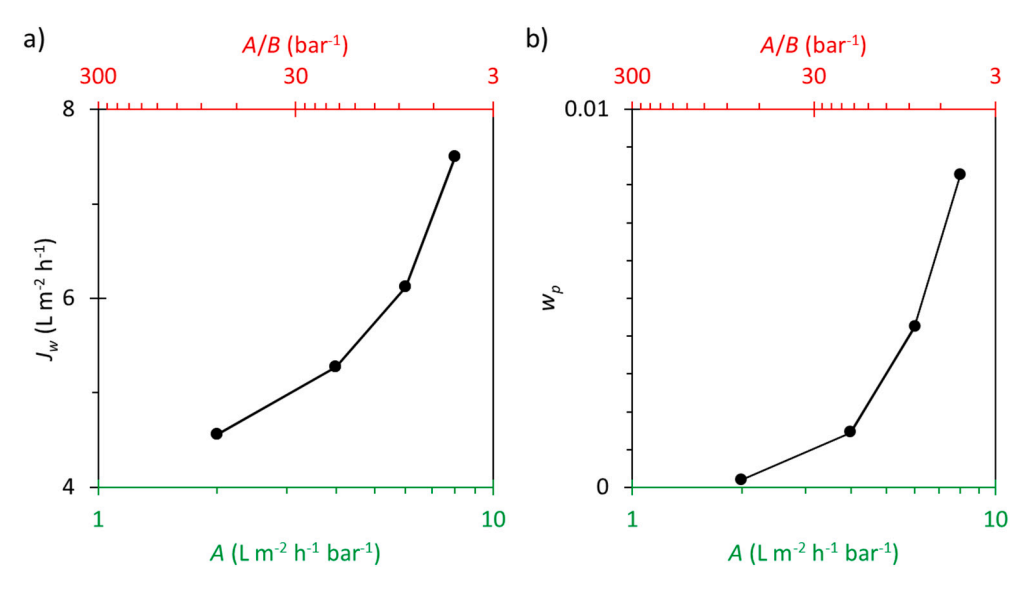


Fig. 8. Dependence of (a) J_w and (b) w_D on A and A/B.

Table 7Validation of existing analytical model reported in literature.

Reference	Output	Input Parameters	Geometry	Main findings
Chen, et al. [10]	Water flux	Pressure 6.9 to 27.6 bars Feed solute fraction 0.0015 to 0.16 Draw solute fraction 0 to 0.13	Rectangular channel	The authors claimed that the analytical result agrees well with the experimental result in terms of water flux. Nevertheless, the deviation of flux between the analytical model and experimental results is higher at a higher Δp due to the constraints in getting an accurate value of B .
Kim, et al. [12]	Water flux	Pressure 0 to 15 bars	Rectangular channel	The authors claimed that the analytical result agrees well with the experimental result in term of water flux.
Chang Kim and Min [11]	Water flux	Pressure 0 to 40 bars Feed solute fraction 0 to 0.067 Draw solute fraction 0 to 0.067	Rectangular channel	The authors claimed that the analytical result agrees well with the experimental result in term of water flux. Nevertheless, the flux predicted by analytical model is higher than experiment results at a higher Δp because of the change in structural parameter under pressurization.
Togo, et al. [13]	Water flux	Pressure 8 to 18 bars Feed solute fraction 0.029 to 0.056	Hollow fiber	The authors claimed that the analytical result agrees well with the experimental result in term of water flux.

pressure to maintain the same recovery [16].

A recent study [41] has investigated the effects of operating conditions on the CP through CFD. It has been found that ECP on the feed side can be more severe than ICP within the porous support layer, particularly at high Δp (>40 bars). Furthermore, significant ECP has been

observed at the draw side of OARO at high Δp . In addition, under the same π_b , an increase in feed solute mass fractions (from 0.034 to 0.083) and draw solute mass fraction (from 0.029 to 0.078) decreases the water flux. This occurs due to the elevated CP, particularly ICP, causing an increase of $\pi_{\rm eff}$. This study also reveals that both the counter-current and co-current systems give comparable flux. In a scaled-up system involving multiple membrane stages, the counter-current configuration is likely to outperform than co-current configuration because it maintains more uniform driving force and flux [69].

Apart from optimizing operating conditions, choice of membrane properties is another factor that needs to be considered for optimizing OARO performance. For example, using a membrane with high water permeability is preferable to a membrane with high solute selectivity in an OARO system because the former can achieve the same recovery at a lower energy requirement [14]. This agrees with the findings reported in Section 2.4.2, where a membrane with high permeability is favored over a highly selective membrane for OARO. However, this principle may not remain valid in systems containing multiple solute species. This is because RSF can occur when the concentration of certain solute species on the draw side exceeds that on the feed side. In such cases, a high-selectivity membrane is required to minimize RSF.

Furthermore, a smaller membrane structural parameter can mitigate the effect of ICP, enhancing the flux and reducing the specific energy consumption [15,16]. However, the specific energy consumption decreases asymptotically as the structural parameter decreases [15]. This is because, when the structural parameter becomes sufficiently small, the mass transfer resistance caused by ICP becomes almost insignificant compared with that caused by ECP. At this point, further reduction in the structural parameter does not lead to significant performance gains. Moreover, with the current membrane manufacturing technology, it is still challenging to make a very thin and strong membrane. Thus, achieving a balance between these factors is crucial. Table 8 summarizes the OARO parametric studies reported in literature.

3.3. Mathematical model for comparing different OARO configurations performance

Traditional RO is a highly energy-intensive system that requires significant transmembrane pressure to overcome the osmotic pressure between channels. In contrast, a smaller transmembrane pressure can be applied in a OARO multistage system. Studies comparing both RO and OARO processes have demonstrated that OARO has a lower unit cost of water production [4,16]. It was reported elsewhere that OARO (\$0.984/

Table 8Mathematical model for OARO parametric studies reported in literature.

Reference	Operating parameters	Parameter variation	Main findings
Bartholomew, et al. [3]	Membrane area per module	9 to 13 m ²	An increase in the membrane area per module can reduce the number of modules required, decreasing the energy consumption.
	Transmembrane pressure	55 to 75 bars	To achieve the same water recovery, increasing the Δp can reduce the number of stages required, leading to less energy consumption.
Park, et al. [16]	Ratio of draw to feed inlet flow rates	0.2 to 1.8	An increase in flow rate ratio increases the SEC of whole system. Nevertheless, if the flow rate ratio is lower, the draw solute fraction decreases more significantly, requiring higher transmembrane pressure to overcome the osmotic pressure difference.
	Structural parameter	50 to 300 μm	A smaller membrane structure parameter reduces the effect of ICP.
Peters and Hankins [14]	Water permeability	1.13 to 6.25 L m^{-2} h^{-1} bar $^{-1}$	A membrane with high water permeability is more beneficial for OARO than one with high selectivity, as it requires less energy consumption to achieve the same level of recovery.
	Flow rate	4 to 12 m ³ h ⁻¹	Lower flowrate results in higher water recovery and lower energy consumption, but also results in a higher capital cost and higher tendency of fouling.
	Ratio of draw to feed inlet flow rates	0.5 to 1.5	Lower ratio of draw inlet flow rate to feed inlet flow rate is more practical to prevent excessive pressure losses in the draw channel.
Bouma and Lienhard [15]	Flux	0 to 30 L m ⁻² h ⁻¹	Operating at high fluxes can intensify CP, necessitating the need of a higher pressure to achieve the desired flux.
	Solute permeability	0.01 to 10 L $$m^{-2}\>h^{-1}$$	A higher solute permeability membrane results in less severe ICP.
	Structural parameter	10 to 1000 μm	A smaller membrane structure parameter can reduce the effect of ICP.
Chong, et al. [41]	Transmembrane pressure	13.8 to 48.3 bars	In situations involving high transmembrane pressure, ECP on feed side is more significant than ICP. Furthermore, ECP on the draw side is non-negligible.
	Feed solute fraction	0.034 to 0.083	Counter and co-current OARO configuration give comparable flux performance.

Table 8 (continued)

Reference	Operating parameters	Parameter variation	Main findings
	Draw solute fraction Flow rate Flow direction	0.017 to 0.078 0.12 to 0.19 m s ⁻¹ Co- and counter current	Under the same bulk osmotic pressure difference, an increase in feed solute mass fractions and draw solute mass fraction decreases the water flux due to the elevated ICP.

 m^3) can reduce the unit water cost up to 10 % compared with traditional RO (\$1.098/ m^3) in treating seawater (3.5 wt% salinity) [16]. For a higher saline brine (ranging from 5 to 12.5 wt%), the optimal OARO configuration with water recoveries of 30 to 70 % requires a cost of maximum \$6/ m^3 [4].

The multistage OARO system was first proposed by Bartholomew, et al. [3] as shown in Fig. 9a. This configuration is also known as consecutive loop configuration or CL-OARO. Using the CL-OARO configuration, the water from the hypersaline feed is extracted and permeates to the draw side to dilute its concentration, in which the resulting diluted draw solution is used as the feed for the next OARO module. This dilution process is repeated until the solution can be effectively treated by traditional RO which is placed at the last stage of CL-OARO. They found that CL-OARO could achieve a water recovery rate of 35 to 50 % with an energy consumption of 6 to 19 kWh/m³ for a 10 to 14 wt% NaCl solution.

For cascading osmotically mediated reverse osmosis (COMRO), on the other hand, the brine feed to the OARO is sourced from the brine stream of RO (see Fig. 9b) [18]. This configuration consumes at least 17 % lower energy compared with traditional RO. It is also worth noting that COMRO can be integrated with the FO [19] to form a FO-COMRO hybrid system (Fig. 9c). This hybrid system can recover 75 % of water from metallurgical wastewater using 20 wt% NaCl draw solution which is then regenerated using COMRO at the cost of 6.05 \$/m³ and energy consumption of 7.4 kWh/m³. Atia, et al. [70] reported that CL-OARO is more energy efficient than COMRO (10.3 kWh/m³ in CL-ORAO versus 12.8 kWh/m³ in COMRO). In addition, the levelized cost of water was also lower for the CL-OARO configuration compared with the COMRO (\$5.14/m³ vs \$7.90/m³) [70].

Nevertheless, CL-OARO has certain limitations, wherein the amount of water and salt entering each loop must be equal to the amount exiting the loop to maintain a steady state [3,15]. If these salt fluxes are not equal, salt will either accumulate or be depleted within a loop, adversely affecting the system's performance. It should be noted that while the water flux can be adjusted by manipulating hydraulic pressure, controlling the same salt flux into and out of each loop is much more challenging. In contrast, COMRO does not have this limitation, as it does not form a loop system. To overcome these abovementioned limitations, a make-up stream is required to maintain the steady operation and to balance the flow rates between the feed and draw sides.

A portion of feed or brine can be split and recirculated into the OARO system as a make-up stream. The configuration that splits a portion of feed is known as split-feed OARO (SF-OARO) [15] (see Fig. 9d), whereas the configuration that splits brine is known as split-brine OARO (SB-OARO) [20,21] (Fig. 9e). When comparing SB-OARO and SF-OARO, SB-OARO performs better than SF-OARO in terms of SEC (8.66 kWh/m³ vs. 9.47 kWh/m³) and unit water cost (\$3.44/m³ vs \$3.63/m³) [20]. This is because SB-OARO requires fewer stages to dilute the draw solution to the solute fraction (0.05 wt%) that can be treated using traditional RO and to concentrate the feed solution to the targeted solute fraction (from 7 to 23.4 wt%). Similar findings were reported elsewhere [21], that the SB-OARO system was the most efficient and economical configuration for extracting water from 10 wt% feed and producing 30 wt% brine, outperforming other configurations (i.e., CL- and SF-OARO) in terms of

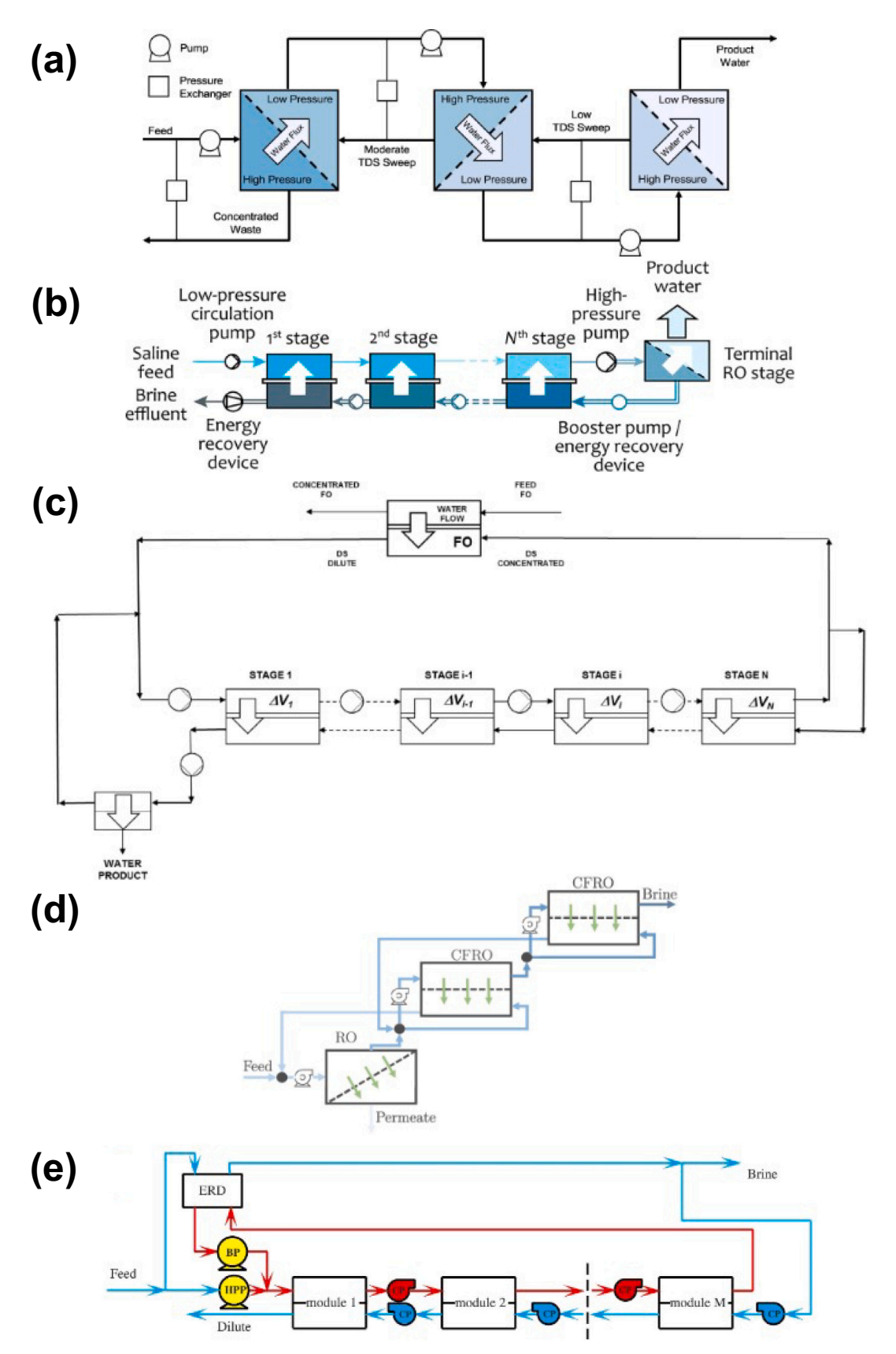


Fig. 9. Different OARO configurations: (a) CL-OARO [3], (b) COMRO [18], (c) FO-COMRO [19], (d) SF-OARO [15], and (e) SB-OARO [20].

treatment cost, membrane area, and energy consumption, owing to the fewer stages and lower pumping energy required. Table 9 summarizes the OARO configurations reported in literature.

4. Future research prospects

4.1. Mathematical model

4.1.1. Development of OARO module-scale model

System-level modeling that simulates the whole process is important for membrane desalination because module-scale experiment requires a huge resource allocation. The system-level modeling of the membrane module-scale can be achieved using the multi-scale model developed in Section 2.3, which combines both a CFD model at small-scale (submillimeter) and analytical model at large-scale (meter).

It is important to recognize the nonlinearity when extrapolating findings from a laboratory-scale to a scaled-up system. This discrepancy arises because, in the case of a very short membrane length, the draw solution experiences only a minor dilution (a few percent). In contrast, in a scaled-up system, the draw solution undergoes substantial dilution, resulting in a significant reduction in both osmotic pressure and flux along the membrane.

Furthermore, despite some existing generalized Sh-correlations used

Table 9

Comparison between different OARO configurations reported in literature.

Companison between	i umerenii OARO (configurations reported in literature.
Reference	Configuration	Main findings
Bartholomew, et al. [3]	CL-OARO	CL-OARO can achieve a water recovery rate of 35 to 50 % with an energy consumption of 6 to 19 kWh/m³ for a 10 to 14 wt% NaCl solution.
Bartholomew, et al. [4]	CL-OARO	The optimal CL-OARO configuration requires cost of only \$6/m³ or less for feed salinity ranges from 5 to 12.5 wt% with achievable water recoveries from 30 to 70 %.
Chen and Yip [18]	COMRO	COMRO consumes less energy by at least 17 % compared with traditional RO.
Martínez, et al. [19]	FO-COMRO	FO-COMRO can recover 75 % of water from metallurgical wastewater using 20 wt% NaCl draw solution which is then regenerated using COMRO at the cost of 6.05 \$/m ³ and energy consumption of 7.4 kWh/m ³ .
Bouma and Lienhard [15]	SF-OARO	SF-OARO can achieve higher water recovery than traditional RO (80 % vs. 60 %). SF-OARO requires 70 bars to concentrate 3.5 wt% feed solution to 20 wt%, whereas traditional RO requires 180 bars to accomplish the same.
Atia, et al. [70]	COMRO & CLOARO	The SEC for COMRO and CL-OARO configurations were 12.8 and 10.3 kWh/m³, respectively. The levelized cost of water for COMRO and CL-OARO configurations were 7.90 and 5.14 \$/m³, respectively.
Beni, et al. [20]	SB- and SF- OARO	The SEC for SB-OARO and SF-OARO configurations to dewater 7 wt% feed to 23.4 wt% were 8.66 and 9.47 kWh/m³, respectively. The unit water cost for SB-OARO and SF-OARO configurations to dewater 7 wt% feed to 23.4 wt% were 3.44 and 3.63 \$/m³, respectively.
Shamlou, et al. [21]	SB-, CL and SF- OARO	SB-OARO system with treatment cost of 5.1 US \$/m³ of produced water with 10 wt% salinity outperforms other configurations (i.e., consecutive loops and split-feed) in terms of number of stages needed, treatment cost, membrane area, and energy consumption.

for OARO (as discussed in Section 2.3), they are valid only for a flat plate [42], feed side channel [43,44] or short membrane length [42]. Therefore, using these correlations for a spacer-filled channel without validation can lead to inaccurate predictions as the presence of spacers significantly increases friction loss and mass transfer. This means opportunities for developing 2D or 3D models for OARO system, which not only help to elucidate the mechanisms involved, but also facilitate the analysis of the system performance when integrated with the analytical model at a large scale. The developed model can also be compared against the available pilot or full-scale real plant data.

4.1.2. Analytical model for optimal control and optimization of large-scale OARO

Process optimization and control is crucial for a membrane-based system to reduce SEC and to achieve a lower operating cost. In a steady continuous cross flow membrane process, the solute concentration as well as the osmotic pressure in the feed increases as it flows along the channel. This results in a varying driving force, which causes a variation in the water flux. Additionally, a high flux membrane system (i.e., high membrane permeance) can cause a rapid reduction of the feed flow rate [71]. Consequently, the highest flux is observed at the beginning of the module, while the lowest flux is at the end, which may negatively impact the energy efficiency of the membrane system. Therefore, finding approaches to ensure a more uniform flux distribution across membrane systems is desirable.

Recently, batch operation has been applied to the OARO [72] which shows promising results in achieving high seawater recovery (60 %) and reducing energy consumption by 30 % compared with continuous OARO process. However, the downtime for flushing and refilling steps were not considered in their model [72], which can decrease the efficiency of this operation. Optimizing cycle reset would be an intriguing research topic for batch operation of OARO. Moreover, batch operation requires a larger membrane area to achieve the same recovery as a continuous OARO operation [72], which can result in an increased capital cost.

One of the methods that can be used for process optimization involves machine learning (ML), which uses existing data obtained from experiments and model solutions [73,74] to train a model that can then be used to predict the best operating conditions and membrane properties. By utilizing ML algorithms, researchers can analyze vast databases of material properties and structures to understand structureproperty relationships, predict material behavior under different conditions, and even propose entirely new material compositions that might exhibit superior properties. Despite the availability of the open access database for membranes [56], ML techniques have not yet been applied. In the context of the membrane open access database, ML could be used for: 1) identifying patterns, correlations, and trends; 2) generating predictive models to forecast membrane performance; 3) recommending membranes for specified conditions; 4) detecting anomalies in a membrane dataset, or 5) determining the best combination of membrane properties (material, thickness, pore size) to meet an objective function. One more notable gap in the open access database research is the lack of utilization of machine learning techniques for predicting specific energy consumption or the economic processing cost, both of which are important metrics in the field of desalination.

Furthermore, the ML model can potentially be used to analyze the spatial and temporal data obtained from CFD to predict how different spacer designs will affect pressure drop, wall shear stress, and mass transfer. In terms of system level modeling, the ML model can be trained to find the optimal combination of operating conditions (pressure, flow rate, temperature, etc.) that maximizes water recovery while minimizing energy consumption [75]. This could accelerate innovation in the OARO membrane technology, as machine learning can handle and process massive amounts of data, resulting in reduced resource requirements and less time compared with the traditional experimental and mathematical simulation approaches. However, it is worth noting that the accurate predictions from machine learning techniques can be

limited if there is not sufficient high-quality data to train the model.

4.2. CFD

4.2.1. CFD for designing improved and mechanical stable draw side spacer For OARO, the draw spacer should be strong enough to withstand the high transmembrane pressure applied at the feed side. Therefore, the volume ratio of spacer-to-channel in the draw channel must be relatively higher than that in the feed channel, which also means that the former has a lower porosity than the latter.

The most common spacer used in the draw side to date is of tricot type [49]. Although this type of spacer provides great support for OARO on the draw side, the effectiveness of mixing using this spacer is highly questionable as it was shown in the recent literature [76,77] that the spacer with most obstructions is not optimal. In addition, the tricot spacer can also cause a large pressure loss inside the channel due to its high flow obstruction nature, which in turn leads to a higher pumping energy. Thus, there is a research opportunity to design a draw spacer that exhibits high mechanical strength, low pressure loss and improved mixing capability.

The spacer performance can be effectively analyzed using CFD [48]. CFD can elucidate various factors influenced by the spacer within the membrane channel, including flow pattern, pressure distribution, and mass transfer. Furthermore, CFD can identify the vortices generated by the spacer that promote mixing at the boundary layer through the lambda-2 criterion [48]. Therefore, CFD has been widely used to access various spacer performances in terms of pressure loss and mass transfer [78,79]. Although it is possible to model the mechanical deformation of a substance through a finite element method (FEM) model and couple it with CFD to simulate the fluid dynamics [80], this method is still not commonly used to assess the mechanical strength of the spacer.

The importance of 3D impacts can be assessed by CFD over a broad range of spacer types, as reported by Fimbres-Weihs and Wiley [81]. One of the important discussions is the relative significance of 3D impacts caused by the feed spacer (typically net-type) versus the draw spacer (typically tricot-type). It is anticipated that the 3D impacts caused by the draw spacer are relatively less important compared with those caused by the feed spacer, due to the fact that the dilutive ECP (DECP) contribution to the effective osmotic pressure is smaller compared with concentrative ECP (CECP) contribution (i.e., 2–9 % for DECP vs 8–38 % for CECP [411]).

Subsequently, the optimization of spacer geometry can also be facilitated by the use of machine learning techniques, in which a surrogate model [82] trained on the obtained CFD data can be used to predict the best spacer design in terms of optimal mixing and low pressure drop. While providing useful insights, the reliability of the machine learning model will be limited by how closely the surrogate model matches an operating OARO system in which there can be many unknown interactions from minor components in the feed water as well as performance deviations introduced by local variations in the membrane and spacer characteristics.

4.2.2. CFD for simulating fouling

Simulating fouling phenomena (i.e., biofouling, particulate fouling, organic fouling, and inorganic scaling) in a membrane process is a challenging task that requires a good understanding of fouling mechanisms. However, there have been no reported fouling simulation studies for OARO to date.

Despite this absence of studies, it is possible to use an existing CFD fouling model obtained from other membrane processes (i.e., FO and RO) in OARO process. For example, biofouling can be governed by Monod kinetics [83] and modeled via sliding meshes [84], which may elucidate the growth of biofilm thickness at different time steps. The reaction rate parameters of Monod kinetics can be determined through experiments conducted in membrane modules and activated sludge models [85]. The mass balance of the biomass, including the transport,

growth, decay, attachment and detachment can be modeled the via discrete cellular automata biofilm model [86].

The scaling, on the other hand, can be modeled by using a particle-based approach [87] which could elucidate the growth of nuclei to a critical size, segregation and formation of new nuclei and particle compaction and immobilization. The nucleation rate can be determined by classical nucleation theory [88], which is expressed as a function of the local degree of saturation in the solution. Then, the nuclei grow to the critical size, governed by the crystal growth rate [89], and split into two smaller particles to form new nuclei.

Lastly, the particulate fouling can be modeled via a Lagrangian approach [90] in order to elucidate the particle trajectory and deposition inside the spacer-filled membrane channel. Nevertheless, studies on the combination of different types of fouling are still limited due to the complex interaction between individual foulants that contribute to the fouling development.

5. Conclusion

Within the last six years, OARO has been studied as an alternative to recover more water from hypersaline water due to the fact that the conventional RO application is limited by the maximum transmembrane pressure (Δp). This paper establishes CFD methodologies for small-scale modeling to elucidate local hydrodynamic and mass transfer and presents how knowledge from the local transport phenomena can be applied to system-level analysis at the module-scale. Furthermore, this paper outlines some prospective future research directions, such as the development of module-scale modeling, machine learning, optimization of spacer geometry and fouling models for enhancing OARO system performance. The following are the key takeaways from this review:

- To date, analytical models were used for most of the process design but the CFD model related to OARO has received very little attention. Thus, CFD methodologies for simulating OARO processes using classical ICP and Brinkman porous media approaches together with validation and sensitivity analysis are demonstrated in this review. The validation shows that both classical ICP and Brinkman models demonstrate good agreement with reported experimental water flux measurements. The sensitivity analysis shows that the variations in membrane properties do not cause significant differences in flux between both approaches, except for the membrane thickness. This is due to the fact that the classical ICP model does not consider the viscous drag in the porous media, leading to negligible flow resistance which overpredicts the permeate velocity.
- The current osmotic membrane is still not optimal for OARO. Due to the trade-off between the membrane permeability and selectivity, the membrane community is currently facing a dilemma in prioritizing whether the membrane permeability or selectivity for OARO should be optimized. This study simulated the OARO operations using membrane with different permeability and selectivity parameters and found that membrane with a high permeability is preferred over a highly selective membrane for OARO. However, this principle may not hold true for systems with multiple solute species. This is because RSF can occur when the concentration of certain solute species on the draw side exceeds that found on the feed side. In such cases, a high-selectivity membrane is necessary to minimize RSF. Further studies are needed to close this gap.
- OARO can achieve lower unit water cost than traditional RO in treating highly saline feed. This is because a lower transmembrane pressure is required in OARO. Various possible OARO configurations have been proposed to optimize this innovative process. To date, the split brine-OARO system is regarded as the most efficient and economical configuration. Furthermore, some novel OARO configurations (i.e., batch) have been reported to overcome the issue of decreasing water flux over time by replenishing the feed and draw with new solution to maintain a consistent driving force, which

eliminates the need to increase the applied pressure as time passes and to ensure a steady water flux.

- Some of the current correlations used for OARO are limited in their applicability, either being only valid for the feed side channel or applicable only for short membrane lengths. To advance the understanding of the mechanisms involved in OARO, future research should focus on developing a comprehensive CFD model for OARO, in which its correlation at small-scale (submillimeter) can be transferred to system-level model (meter scale) via multi-scale model approach.
- Traditionally, the optimization of membrane processes involves experimental or numerical trial and error methods that are time-consuming and expensive. However, with the advancement of data-driven method (e.g., machine learning), it is now possible to optimize the membrane process more efficiently and accurately at all scales, such as predicting the membrane materials and structures with superior properties (nanoscale), designing a spacer geometry with enhanced mixing and minimal pressure loss performances (submillimeter) and optimizing the operating conditions to obtain the maximum water recovery and the minimum energy consumption (meter-scale). This research field is anticipated to become more prominent in the coming years, as machine learning techniques continue to improve and become more accessible.
- The simulation of combined fouling has yet to be fully explored in CFD to elucidate the transient fouling development phenomena. To bridge this gap, more efforts are needed to develop a deeper mathematical understanding of the interaction of various fouling mechanisms in a CFD code.

Declaration of competing interest

The authors declare that they have no known competing financial interests or personal relationships that could have appeared to influence the work reported in this paper.

Data availability

Data will be made available on request.

Acknowledgements

The authors would like to thank the Ministry of Higher Education for providing financial support under Fundamental Research Grant Scheme (FRGS) No. FRGS/1/2023/TK05/UMP/02/3 (University reference RDU230120).

Appendix A. Supplementary data

Supplementary data to this article can be found online at https://doi.org/10.1016/j.desal.2024.117893.

References

- [1] C. Fritzmann, J. Löwenberg, T. Wintgens, T. Melin, State-of-the-art of reverse osmosis desalination, Desalination 216 (2007) 1–76.
- [2] S. Loeb, M.R. Bloch, Countercurrent flow osmotic processes for the production of solutions having a high osmotic pressure, Desalination 13 (1973) 207–215.
- [3] T.V. Bartholomew, L. Mey, J.T. Arena, N.S. Siefert, M.S. Mauter, Osmotically assisted reverse osmosis for high salinity brine treatment, Desalination 421 (2017) 3–11.
- [4] T.V. Bartholomew, N.S. Siefert, M.S. Mauter, Cost optimization of osmotically assisted reverse osmosis, Environ. Sci. Technol. 52 (2018) 11813–11821.
- [5] M.M. Zubair, H. Saleem, S.J. Zaidi, Recent progress in reverse osmosis modeling: an overview, Desalination 564 (2023) 116705.
- [6] A. Katchalsky, O. Kedem, Thermodynamics of flow processes in biological systems, Biophys. J. 2 (1962) 53–78.
- [7] K.S. Spiegler, O. Kedem, Thermodynamics of hyperfiltration (reverse osmosis): criteria for efficient membranes, Desalination 1 (1966) 311–326.
- [8] Y.Y. Liang, Review of analytical and numerical modeling for pressure retarded osmosis membrane systems, Desalination 560 (2023) 116655.

[9] R.R. Gonzales, K. Nakagawa, K. Kumagai, S. Hasegawa, A. Matsuoka, Z. Li, Z. Mai, T. Yoshioka, T. Hori, H. Matsuyama, Hybrid osmotically assisted reverse osmosis and reverse osmosis (OARO-RO) process for minimal liquid discharge of high strength nitrogenous wastewater and enrichment of ammoniacal nitrogen, Water Res. 246 (2023) 120716.

- [10] X. Chen, C. Boo, N.Y. Yip, Transport and structural properties of osmotic membranes in high-salinity desalination using cascading osmotically mediated reverse osmosis, Desalination 479 (2020) 114335.
- [11] Y. Chang Kim, T. Min, Influence of osmotic mediation on permeation of water in reverse osmosis: experimental and numerical analysis, J. Membr. Sci. 595 (2020) 117574.
- [12] J. Kim, D.I. Kim, S. Hong, Analysis of an osmotically-enhanced dewatering process for the treatment of highly saline (waste)waters, J. Membr. Sci. 548 (2018) 685–693.
- [13] N. Togo, K. Nakagawa, T. Shintani, T. Yoshioka, T. Takahashi, E. Kamio, H. Matsuyama, Osmotically assisted reverse osmosis utilizing hollow fiber membrane module for concentration process, Ind. Eng. Chem. Res. 58 (2019) 6721_6729
- [14] C.D. Peters, N.P. Hankins, Osmotically assisted reverse osmosis (OARO): five approaches to dewatering saline brines using pressure-driven membrane processes, Desalination 458 (2019) 1–13.
- [15] A.T. Bouma, J.H. Lienhard, Split-feed counterflow reverse osmosis for brine concentration, Desalination 445 (2018) 280–291.
- [16] K. Park, D.Y. Kim, D.R. Yang, Cost-based feasibility study and sensitivity analysis of a new draw solution assisted reverse osmosis (DSARO) process for seawater desalination, Desalination 422 (2017) 182–193.
- [17] Z. Mo, C.D. Peters, C. Long, N.P. Hankins, Q. She, How split-feed osmotically assisted reverse osmosis (SF-OARO) can outperform conventional reverse osmosis (CRO) processes under constant and varying electricity tariffs, Desalination 530 (2022) 115670.
- [18] X. Chen, N.Y. Yip, Unlocking high-salinity desalination with cascading osmotically mediated reverse osmosis: energy and operating pressure analysis, Environ. Sci. Technol. 52 (2018) 2242–2250.
- [19] J. Martínez, E. León, F.M. Baena-Moreno, M. Rodríguez-Galán, F. Arroyo-Torralvo, L.F. Vilches, Techno-economic analysis of a membrane-hybrid process as a novel low-energy alternative for zero liquid discharge systems, Energy Convers. Manag. 211 (2020) 112783.
- [20] A.N. Beni, I. Ghofrani, A. Moosavi, On comparison of three multi-feed osmotic-mediation-based configurations for brine management: techno-economic optimization and exergy analysis, Desalination 525 (2022) 115517.
- [21] E. Shamlou, R. Vidic, M.M. El-Halwagi, V. Khanna, Optimization-based modeling and analysis of brine reflux osmotically assisted reverse osmosis for application toward zero liquid discharge systems, Desalination 539 (2022) 115948.
- [22] S. Loeb, L. Titelman, E. Korngold, J. Freiman, Effect of porous support fabric on osmosis through a Loeb-Sourirajan type asymmetric membrane, J. Membr. Sci. 129 (1997) 243–249.
- [23] M.A. Al-Obaidi, A.A. Alsarayreh, A.M. Al-Hroub, S. Alsadaie, I.M. Mujtaba, Performance analysis of a medium-sized industrial reverse osmosis brackish water desalination plant, Desalination 443 (2018) 272–284.
- [24] Y.K. Goi, Y.Y. Liang, Impact of temperature and forward osmosis membrane properties on the concentration polarization and specific energy consumption of hybrid desalination system, Environ. Sci. Pollut. Res. 31 (2024) 32246–32263.
- [25] T.V. Bartholomew, M.S. Mauter, Computational framework for modeling membrane processes without process and solution property simplifications, J. Membr. Sci. 573 (2019) 682–693.
- [26] W.N. Gill, D.E. Wiley, C.J.D. Fell, A.G. Fane, Effect of viscosity on concentration polarization in ultrafiltration, AICHE J. 34 (1988) 1563–1567.
- [27] D.F. Fletcher, D.E. Wiley, A computational fluids dynamics study of buoyancy effects in reverse osmosis, J. Membr. Sci. 245 (2004) 175–181.
- [28] B. Kim, G. Gwak, S. Hong, Review on methodology for determining forward osmosis (FO) membrane characteristics: water permeability (A), solute permeability (B), and structural parameter (S), Desalination 422 (2017) 5–16.
- [29] J.R. McCutcheon, M. Elimelech, Influence of concentrative and dilutive internal concentration polarization on flux behavior in forward osmosis, J. Membr. Sci. 284 (2006) 237–247.
- [30] T.Y. Cath, M. Elimelech, J.R. McCutcheon, R.L. McGinnis, A. Achilli, D. Anastasio, A.R. Brady, A.E. Childress, I.V. Farr, N.T. Hancock, J. Lampi, L.D. Nghiem, M. Xie, N.Y. Yip, Standard methodology for evaluating membrane performance in osmotically driven membrane processes, Desalination 312 (2013) 31–38.
- [31] A. Tiraferri, N.Y. Yip, W.A. Phillip, J.D. Schiffman, M. Elimelech, Relating performance of thin-film composite forward osmosis membranes to support layer formation and structure, J. Membr. Sci. 367 (2011) 340–352.
- [32] J. Wei, C. Qiu, C.Y. Tang, R. Wang, A.G. Fane, Synthesis and characterization of flat-sheet thin film composite forward osmosis membranes, J. Membr. Sci. 372 (2011) 292–302.
- [33] G. Sundaramoorthi, M. Hadwiger, M. Ben-Romdhane, A.R. Behzad, P. Madhavan, S.P. Nunes, 3D membrane imaging and porosity visualization, Ind. Eng. Chem. Res. 55 (2016) 3689–3695.
- [34] A. Ley, P. Altschuh, V. Thom, M. Selzer, B. Nestler, P. Vana, Characterization of a macro porous polymer membrane at micron-scale by Confocal-Laser-Scanning Microscopy and 3D image analysis, J. Membr. Sci. 564 (2018) 543–551.
- [35] S.S. Manickam, J. Gelb, J.R. McCutcheon, Pore structure characterization of asymmetric membranes: non-destructive characterization of porosity and tortuosity, J. Membr. Sci. 454 (2014) 549–554.
- [36] S.S. Manickam, J.R. McCutcheon, Understanding mass transfer through asymmetric membranes during forward osmosis: a historical perspective and

- critical review on measuring structural parameter with semi-empirical models and characterization approaches, Desalination 421 (2017) 110–126.
- [37] V.t. Geraldes, V. Semião, M.N. de Pinho, Flow and mass transfer modelling of nanofiltration, J. Membr. Sci. 191 (2001) 109–128.
- [38] G. Scatchard, W.J. Hamer, S.E. Wood, Isotonic solutions. I. The chemical potential of water in aqueous solutions of sodium chloride, potassium chloride, sulfuric acid, sucrose, urea and glycerol at 25°1, J. Am. Chem. Soc. 60 (1938) 3061–3070.
- [39] P.S.Z. Rogers, K.S. Pitzer, Volumetric properties of aqueous sodium chloride solutions, J. Phys. Chem. Ref. Data Monogr. 11 (1982) 15–81.
- [40] K.L. Lee, R.W. Baker, H.K. Lonsdale, Membranes for power generation by pressureretarded osmosis, J. Membr. Sci. 8 (1981) 141–171.
- [41] Y.K. Chong, D.F. Fletcher, Y.Y. Liang, CFD simulation of hydrodynamics and concentration polarization in osmotically assisted reverse osmosis membrane systems, J. Water Process Eng. 57 (2024) 104535.
- [42] S. Kim, E.M.V. Hoek, Modeling concentration polarization in reverse osmosis processes, Desalination 186 (2005) 111–128.
- [43] G. Guillen, E.M.V. Hoek, Modeling the impacts of feed spacer geometry on reverse osmosis and nanofiltration processes, Chem. Eng. J. 149 (2009) 221–231.
- [44] C.P. Koutsou, S.G. Yiantsios, A.J. Karabelas, A numerical and experimental study of mass transfer in spacer-filled channels: effects of spacer geometrical characteristics and Schmidt number, J. Membr. Sci. 326 (2009) 234–251.
- [45] G. Schock, A. Miquel, Mass transfer and pressure loss in spiral wound modules, Desalination 64 (1987) 339–352.
- [46] P.K. Kang, W. Lee, S. Lee, A.S. Kim, Origin of structural parameter inconsistency in forward osmosis models: a pore-scale CFD study, Desalination 421 (2017) 47–60.
- [47] T.J. Barth, Aspects of Unstructured Grids and Finite-Volume Solvers for the Euler and Navier-Stokes Equations, AGARD, Special Course on Unstructured Grid Methods for Advection Dominated Flows, 1992.
- [48] Y.K. Chong, Y.Y. Liang, G.A.F. Weihs, Validation and characterisation of mass transfer of 3D-CFD model for twisted feed spacer, Desalination 554 (2023) 116516.
- [49] A.P. Straub, N.Y. Yip, M. Elimelech, Raising the bar: increased hydraulic pressure allows unprecedented high power densities in pressure-retarded osmosis, Environ. Sci. Technol. Lett. 1 (2014) 55–59.
- [50] Z. Wang, J. Tang, C. Zhu, Y. Dong, Q. Wang, Z. Wu, Chemical cleaning protocols for thin film composite (TFC) polyamide forward osmosis membranes used for municipal wastewater treatment, J. Membr. Sci. 475 (2015) 184–192.
- [51] N.Y. Yip, A. Tiraferri, W.A. Phillip, J.D. Schiffman, M. Elimelech, High performance thin-film composite forward osmosis membrane, Environ. Sci. Technol. 44 (2010) 3812–3818.
- [52] A. Sagiv, A. Zhu, P.D. Christofides, Y. Cohen, R. Semiat, Analysis of forward osmosis desalination via two-dimensional FEM model, J. Membr. Sci. 464 (2014) 161–172.
- [53] A. Sagiv, P.D. Christofides, Y. Cohen, R. Semiat, On the analysis of FO mass transfer resistances via CFD analysis and film theory, J. Membr. Sci. 495 (2015) 198–205.
- [54] N. Niknafs, A. Jalali, Performance analysis of cross-flow forward osmosis membrane modules with mesh feed spacer using three-dimensional computational fluid dynamics simulations, Chem. Eng. Process. Process Intensif. 168 (2021) 108583
- [55] M. Askari, C.Z. Liang, L.T. Choong, T.-S. Chung, Optimization of TFC-PES hollow fiber membranes for reverse osmosis (RO) and osmotically assisted reverse osmosis (OARO) applications, J. Membr. Sci. 625 (2021) 119156.
- [56] C.L. Ritt, T. Stassin, D.M. Davenport, R.M. DuChanois, I. Nulens, Z. Yang, A. Ben-Zvi, N. Segev-Mark, M. Elimelech, C.Y. Tang, G.Z. Ramon, I.F.J. Vankelecom, R. Verbeke, The open membrane database: synthesis-structure-performance relationships of reverse osmosis membranes, J. Membr. Sci. 641 (2022) 119927.
- [57] X. Lu, M. Elimelech, Fabrication of desalination membranes by interfacial polymerization: history, current efforts, and future directions, Chem. Soc. Rev. 50 (2021) 6290–6307
- [58] B. Comesaña-Gándara, J. Chen, C.G. Bezzu, M. Carta, I. Rose, M.-C. Ferrari, E. Esposito, A. Fuoco, J.C. Jansen, N.B. McKeown, Redefining the Robeson upper bounds for CO2/CH4 and CO2/N2 separations using a series of ultrapermeable benzotriptycene-based polymers of intrinsic microporosity, Energy Environ. Sci. 12 (2019) 2733–2740.
- [59] T.H. Chong, S.-L. Loo, W.B. Krantz, Energy-efficient reverse osmosis desalination process, J. Membr. Sci. 473 (2015) 177–188.
- [60] T.H. Chong, S.-L. Loo, A.G. Fane, W.B. Krantz, Energy-efficient reverse osmosis desalination: effect of retentate recycle and pump and energy recovery device efficiencies, Desalination 366 (2015) 15–31.
- [61] Z. Wang, A. Deshmukh, Y. Du, M. Elimelech, Minimal and zero liquid discharge with reverse osmosis using low-salt-rejection membranes, Water Res. 170 (2020) 115317.
- [62] G.M. Geise, H.B. Park, A.C. Sagle, B.D. Freeman, J.E. McGrath, Water permeability and water/salt selectivity tradeoff in polymers for desalination, J. Membr. Sci. 369 (2011) 130–138.
- [63] J.R. Werber, A. Deshmukh, M. Elimelech, The critical need for increased selectivity, not increased water permeability, for desalination membranes, Environ. Sci. Technol. Lett. 3 (2016) 112–120.
- [64] Q. She, X. Jin, C.Y. Tang, Osmotic power production from salinity gradient resource by pressure retarded osmosis: effects of operating conditions and reverse solute diffusion, J. Membr. Sci. 401-402 (2012) 262–273.

[65] F. Yu, H. Shi, J. Shi, K. Teng, Z. Xu, X. Qian, High-performance forward osmosis membrane with ultra-fast water transport channel and ultra-thin polyamide layer, J. Membr. Sci. 616 (2020) 118611.

- [66] L. Shen, X. Zhang, L. Tian, Z. Li, C. Ding, M. Yi, C. Han, X. Yu, Y. Wang, Constructing substrate of low structural parameter by salt induction for highperformance TFC-FO membranes, J. Membr. Sci. 600 (2020) 117866.
- [67] A.S. Al-Amoudi, S. Ihm, A.M. Farooque, E.S.B. Al-Waznani, N. Voutchkov, Dual brine concentration for the beneficial use of two concentrate streams from desalination plant - concept proposal and pilot plant demonstration, Desalination 564 (2023) 116789.
- [68] M. Rahimi, S.S. Madaeni, M. Abolhasani, A.A. Alsairafi, CFD and experimental studies of fouling of a microfiltration membrane, Chem. Eng. Process. Process Intensif. 48 (2009) 1405–1413.
- [69] D. Xiao, W. Li, S. Chou, R. Wang, C.Y. Tang, A modeling investigation on optimizing the design of forward osmosis hollow fiber modules, J. Membr. Sci. 392-393 (2012) 76–87.
- [70] A.A. Atia, N.Y. Yip, V. Fthenakis, Pathways for minimal and zero liquid discharge with enhanced reverse osmosis technologies: module-scale modeling and technoeconomic assessment, Desalination 509 (2021) 115069.
- [71] K.Y. Toh, Y.Y. Liang, W.J. Lau, G.A.F. Weihs, The techno-economic case for coupling advanced spacers to high-permeance RO membranes for desalination, Desalination 491 (2020) 114534.
- [72] A. Das, D.M. Warsinger, Batch counterflow reverse osmosis, Desalination 507 (2021) 115008.
- [73] J. Jawad, A.H. Hawari, S. Javaid Zaidi, Artificial neural network modeling of wastewater treatment and desalination using membrane processes: a review, Chem. Eng. J. 419 (2021) 129540.
- [74] S.H. Chae, S. Moon, S.W. Hong, C. Lee, M. Son, Performance investigation of osmotically assisted reverse osmosis using explainable machine learning models: a comparative study, Desalination 583 (2024) 117647.
- [75] J. Luo, M. Li, E.M.V. Hoek, Y. Heng, Supercomputing and machine learning-aided optimal design of high permeability seawater reverse osmosis membrane systems, Sci. Bull. 68 (2023) 397–407.
- [76] K.Y. Toh, Y.Y. Liang, W.J. Lau, G.A. Fimbres Weihs, 3D CFD study on hydrodynamics and mass transfer phenomena for SWM feed spacer with different floating characteristics, Chem. Eng. Res. Des. 159 (2020) 36–46.
- [77] A.N. Beni, I. Ghofrani, A. Nouri-Borujerdi, A. Moosavi, D.M. Warsinger, Membrane properties overview in integrated forward osmosis/osmotically assisted reverse osmosis systems, Desalination 569 (2023) 117008.
- [78] Y.K. Chong, Y.Y. Liang, W.J. Lau, G.A. Fimbres Weihs, 3D CFD study of hydrodynamics and mass transfer phenomena for spiral wound membrane submerged-type feed spacer with different node geometries and sizes, Int. J. Heat Mass Transf. 191 (2022) 122819.
- [79] W.-c. Lin, R.-p. Shao, X.-m. Wang, X. Huang, Impacts of non-uniform filament feed spacers characteristics on the hydraulic and anti-fouling performances in the spacer-filled membrane channels: experiment and numerical simulation, Water Res. 185 (2020) 116251.
- [80] P. Chippar, K. Oh, D. Kim, T.-W. Hong, W. Kim, H. Ju, Coupled mechanical stress and multi-dimensional CFD analysis for high temperature proton exchange membrane fuel cells (HT-PEMFCs), Int. J. Hydrog. Energy 38 (2013) 7715–7724.
- [81] G.A. Fimbres-Weihs, D.E. Wiley, Review of 3D CFD modeling of flow and mass transfer in narrow spacer-filled channels in membrane modules, Chem. Eng. Process. Process Intensif. 49 (2010) 759–781.
- [82] Z.M. Binger, A. Achilli, Surrogate modeling of pressure loss & mass transfer in membrane channels via coupling of computational fluid dynamics and machine learning, Desalination 548 (2023) 116241.
- [83] J. Monod, The growth of bacterial cultures, Ann. Rev. Microbiol. 3 (1949) 371–394.
- [84] S.S. Bucs, R. Valladares Linares, J.S. Vrouwenvelder, C. Picioreanu, Biofouling in forward osmosis systems: an experimental and numerical study, Water Res. 106 (2016) 86–97.
- [85] C. Picioreanu, J.S. Vrouwenvelder, M.C.M. van Loosdrecht, Three-dimensional modeling of biofouling and fluid dynamics in feed spacer channels of membrane devices, J. Membr. Sci. 345 (2009) 340–354.
- [86] C. Picioreanu, M.C.M. van Loosdrecht, J.J. Heijnen, Mathematical modeling of biofilm structure with a hybrid differential-discrete cellular automaton approach, Biotechnol. Bioeng. 58 (1998) 101–116.
- [87] A.I. Radu, L. Bergwerff, M.C.M. van Loosdrecht, C. Picioreanu, A two-dimensional mechanistic model for scaling in spiral wound membrane systems, Chem. Eng. J. 241 (2014) 77–91.
- [88] J.W. Mullin, 5 nucleation, in: J.W. Mullin (Ed.), Crystallization (Fourth Edition), Butterworth-Heinemann, Oxford, 2001, pp. 181–215.
- [89] A.E. Nielsen, Electrolyte crystal growth mechanisms, J. Cryst. Growth 67 (1984) 289–310.
- [90] A.I. Radu, M.S.H. van Steen, J.S. Vrouwenvelder, M.C.M. van Loosdrecht, C. Picioreanu, Spacer geometry and particle deposition in spiral wound membrane feed channels, Water Res. 64 (2014) 160–176.